



저작자표시-비영리-변경금지 2.0 대한민국

이용자는 아래의 조건을 따르는 경우에 한하여 자유롭게

- 이 저작물을 복제, 배포, 전송, 전시, 공연 및 방송할 수 있습니다.

다음과 같은 조건을 따라야 합니다:



저작자표시. 귀하는 원 저작자를 표시하여야 합니다.



비영리. 귀하는 이 저작물을 영리 목적으로 이용할 수 없습니다.



변경금지. 귀하는 이 저작물을 개작, 변형 또는 가공할 수 없습니다.

- 귀하는, 이 저작물의 재이용이나 배포의 경우, 이 저작물에 적용된 이용허락조건을 명확하게 나타내어야 합니다.
- 저작권자로부터 별도의 허가를 받으면 이러한 조건들은 적용되지 않습니다.

저작권법에 따른 이용자의 권리와 책임은 위의 내용에 의하여 영향을 받지 않습니다.

이것은 [이용허락규약\(Legal Code\)](#)을 이해하기 쉽게 요약한 것입니다.

[Disclaimer](#)



공학석사 학위논문

단일 상승 기포에 의한 수직 열판의 열전달 변화

Variation of wall heat transfer on a vertical heated
wall due to a single rising bubble

2020년 2월

서울대학교 대학원
기계항공공학부
맹 휘 영

Variation of wall heat transfer on a vertical heated wall due to a single rising bubble

Hwiyoung Maeng, Master of Philosophy
Mechanical and Aerospace Engineering
Seoul National University, 2019

Advisor: Prof. Hyungmin Park

Abstract

In the present study, we experimentally investigate the convective heat transfer variation of the vertical heated wall, and establish its mechanism. The temperature field of the vertical heated wall is captured by the infrared camera, and the bubble movement and its wake are measured by the high-speed two-phase particle image velocimetry, where these two cameras are timely synchronized. The temporal-local convective heat transfer increases when a bubble passes near the wall, and by changing the bubble-wall distance and the size of the bubble, we observe the variation of the

heat transfer enhancement. The bubble of which diameter is 2.8 mm moves in the zigzagging path, and the 1.1 mm bubble rises linearly. When the zigzagging bubble impacts on the wall, the instantaneous-local heat transfer increases up to eight times higher, and as the bubble-wall distance gets further, the maximum increment of the instantaneous-local heat transfer decreases exponentially. Here, the maximum velocity components induced near the wall (wall-normal velocity; shear flow velocity) and the maximum vorticity induced near the wall are extracted according to the bubble-wall distance. The relationships between the maximum temporal-local heat transfer enhancement and each intensities of the flow components are verified, and we find out that the wall-normal velocity is the most effective flow component for the surface cooling. Therefore, the main mechanism of the surface cooling is the surface renewal by the entrained bulk liquid to the heated wall. When it is the straight rising bubble, however, the injected bubble is not effective for the surface cooling: when a linearly rising bubble collides with the wall, the enhancement of the instantaneous-local convective heat transfer is less than 10%. Also, when a linearly rising bubble moves without any impingement, there is no cooling effect. Visualizing the wake of a straight rising bubble, we find out that the flow induced by a bubble is slow and the wake size is small, compared to the case of a zigzagging bubble. Based on the laminar free convection boundary layer equations, we roughly get the ratio of the momentum boundary layer thickness and the thermal boundary layer thickness. Moreover, from the measured flow velocity field, we roughly find the thickness of the thermal boundary layer. The wake size of the linearly rising bubble is smaller than the thermal boundary layer thickness, which

means that the straight bubble is not effective for the mixing between the hot liquid near the wall and the bulk liquid. Therefore, to cool the surface efficiently, a bubble should induce the high speed of wall-normal velocity, and the wake size of a bubble should be bigger than the thermal boundary layer thickness.

Keyword : rising bubble, shadow image technique, particle tracking velocimetry, particle image velocimetry, convective heat transfer, Nusselt number

Student Number : 2018–25231

Table of Contents

Abstract	i
Table of Contents.....	iv
List of Tables	vi
List of Figures.....	vii
Chapter 1. Introduction.....	1
Chapter 2. Experimental set-up and procedure	6
2.1. Single bubble rising near a vertical wall	6
2.2. High-speed two-phase particle image velocimetry	8
2.3. Convective heat transfer flux measurement	10
2.4. Laser energy absorbed in the foil (q''_{laser})	12
2.5. Uncertainty	13
Chapter 3. Results and discussion	18
3.1. Zigzagging bubble – global Nusselt number	18
3.2. Zigzagging bubble – local Nusselt number at y^*_{max}	28
3.3. Straight bubble.....	33
Chapter 4. Conclusion.....	67
Bibliography	70

국문 초록 74

List of Tables

Table 2.1. Properties of the foil and the paint.	15
Table 3.1. Pearson correlation coefficient (ρ) and p -value between normalized maximum Nusselt number (Nu^*) and normalized maximum absolute value of wall normal velocity ($ w^* $), vertical velocity ($ v^* $) and vorticity ($ \omega_x^* $) induced near the wall ($0.2d_{eq}$ from the wall) at zigzagging plane ($x = 0$).	37

List of Figures

Figure 2.1. (a) Experimental setup for observing the flow velocity field at ($y - z$) plane and for measuring the temperature field of the foil at ($x - y$) plane, using high-speed two-phase particle image velocimetry and infrared camera. (b) Power supplying system for heating the foil, and measurement systems of the wall temperature field and air-gap temperature. (c) Raw image of the high-speed camera in ($y - z$) plane, when a bubble passes the summit point of the path ($t = 0$). (d) Magnified schematic diagram for defining the bubble information.	16
Figure 2.2. Temperature difference between the infrared camera and the black body, as a function of the black body temperature.....	17
Figure 3.1. (a) Normalized vorticity (ω_x^*) contour image. (b) Boundary of the vortex set by the threshold of $\omega_x^* = 0.1$	38
Figure 3.2. Position of the vortex structures: created near the summit point (●), first below the summit point (▼), first and second above the summit point (■ and ▲, respectively) (a), and bubble trajectory (•••): $S^* = 0.5$ (b), $S^* = 1.5$ (c), $S^* = 2.4$ (d), $S^* = 3.2$ (e), $S^* = 4.5$ (f), $S^* = 5.1$ (g), $S^* = 6.1$ (h), and $S^* = 9.7$ (i). In (b–i), the color contour denotes the normalized wall normal velocity.....	39
Figure 3.3. Temporal normalized spanwise vorticity (ω_x^*) field (a),	

and timely synchronized and normalized Nusselt number (Nu^*) field (b), which are timely synchronized, when bubble–wall distance (S^*) is 0.5 (bubble–wall collision ; zigzag–rising bubble). Here, a helps to describe normalized spanwise vorticity contour level and length of the unit vector, t^* denotes the normalized time, and y_b^* means the normalized vertical location of the bubble.....40

Figure 3.4. Temporal normalized spanwise vorticity (ω_x^*) field (a), and timely synchronized and normalized Nusselt number (Nu^*) field (b), which are timely synchronized, when bubble–wall distance (S^*) is 1.5 (bubble passes near the wall; zigzag–rising bubble). Here, a helps to describe normalized spanwise vorticity contour level and length of the unit vector, t^* denotes the normalized time, and y_b^* means the normalized vertical location of the bubble.....41

Figure 3.5. Temporal normalized spanwise vorticity (ω_x^*) field (a), and timely synchronized and normalized Nusselt number (Nu^*) field (b), which are timely synchronized, when bubble–wall distance (S^*) is 2.4 (bubble passes near the wall ; zigzag–rising bubble). Here, a helps to describe normalized spanwise vorticity contour level and length of the unit vector, t^* denotes the normalized time, and y_b^* means the normalized vertical location of the bubble.....42

Figure 3.6. Temporal normalized spanwise vorticity (ω_x^*) field (a), and timely synchronized and normalized Nusselt number (Nu^*) field (b), which are timely synchronized, when bubble–wall distance (S^*) is 3.2 (bubble passes near the wall ; zigzag–rising bubble). Here, a helps to describe normalized spanwise vorticity contour level and length of the unit vector, t^* denotes the normalized time, and y_b^*

means the normalized vertical location of the bubble.....43

Figure 3.7. Temporal normalized spanwise vorticity (ω_x^*) field (a), and timely synchronized and normalized Nusselt number (Nu^*) field (b), which are timely synchronized, when bubble-wall distance (S^*) is 4.5 (bubble passes near the wall ; zigzag-rising bubble). Here, a helps to describe normalized spanwise vorticity contour level and length of the unit vector, t^* denotes the normalized time, and y_b^* means the normalized vertical location of the bubble.....44

Figure 3.8. Temporal normalized spanwise vorticity (ω_x^*) field (a), and timely synchronized and normalized Nusselt number (Nu^*) field (b), which are timely synchronized, when bubble-wall distance (S^*) is 5.1 (bubble passes near the wall ; zigzag-rising bubble). Here, a helps to describe normalized spanwise vorticity contour level and length of the unit vector, t^* denotes the normalized time, and y_b^* means the normalized vertical location of the bubble.....45

Figure 3.9. Temporal normalized spanwise vorticity (ω_x^*) field (a), and timely synchronized and normalized Nusselt number (Nu^*) field (b), which are timely synchronized, when bubble-wall distance (S^*) is 6.1 (bubble passes near the wall ; zigzag-rising bubble). Here, a helps to describe normalized spanwise vorticity contour level and length of the unit vector, t^* denotes the normalized time, and y_b^* means the normalized vertical location of the bubble.....46

Figure 3.10. Temporal normalized spanwise vorticity (ω_x^*) field (a), and timely synchronized and normalized Nusselt number (Nu^*) field (b), which are timely synchronized, when bubble-wall distance (S^*)

is 9.7 (no heat transfer; zigzag-rising bubble). Here, a helps to describe normalized spanwise vorticity contour level and length of the unit vector, t^* denotes the normalized time, and y_b^* means the normalized vertical location of the bubble.....47

Figure 3.11. Temporal variation of the one-dimensional (at $x = 0$, and $z = 0$) normalized Nusselt number (Nu^*) contour: $S^* = 0.5$ (a), $S^* = 1.5$ (b), $S^* = 2.4$ (c), $S^* = 3.2$ (d), $S^* = 4.5$ (e), $S^* = 5.1$ (f), $S^* = 6.1$ (g), and $S^* = 9.7$ (h).....48

Figure 3.12. Upper (\blacktriangle) and lower (\blacktriangledown) boundary where the heat transfer is enhanced, and mean normalized Nusselt number in affected area (\bullet): $S^* = 0.5$ (a), $S^* = 1.5$ (b), $S^* = 2.4$ (c), $S^* = 3.2$ (d), $S^* = 4.5$ (e), $S^* = 5.1$ (f), and $S^* = 6.1$ (g).....49

Figure 3.13. Normalized vertical width where the Nusselt number is increased: $S^* = 0.5$ (\bullet), $S^* = 1.5$ (\blacktriangle), $S^* = 2.4$ (\blacktriangledown), $S^* = 3.2$ (\blacksquare), $S^* = 4.5$ (\blacklozenge), $S^* = 5.1$ (\circlearrowleft), and $S^* = 6.1$ (\triangle).....50

Figure 3.14. Normalized initial increment time of the Nusselt number (\bullet), the normalized time that the vortex structure starts to contact with the wall (\blacktriangle), and the normalized time when the instantaneous-local Nusselt number is the maximum (\blacksquare) as a function of S^*51

Figure 3.15. Normalized time gradient of the normalized Nusselt number, when the Nusselt number starts to increase, as a function of S^*52

Figure 3.16. The normalized maximum Nusselt number (\bullet), and

normalized maximum strength of the wall normal velocity (\blacktriangle), vertical velocity (\blacktriangledown) and vorticity (\blacksquare) at zigzagging plane ($x = 0$), and fluid motions are measured at $0.2d_{eq}$ from the wall ($z^* = 0.2$), as a function of S^*53

Figure 3.17. Normalized vertical position where the temporal-local Nusselt number or each of the local fluid component is maximized as a function of S^* : Nusselt number (\bullet), strength of the wall normal velocity (\blacktriangle), vertical velocity (\blacktriangledown) and vorticity (\blacksquare) at zigzagging plane ($x = 0$), and fluid motions are measured at $0.2d_{eq}$ from the wall ($z^* = 0.2$).....54

Figure 3.18. Normalized local-temporal Nusselt number (Nu^*) as a function of normalized time (t^*): $S^* = 0.5$ (\bullet), $S^* = 1.5$ (\blacktriangle), $S^* = 2.4$ (\blacktriangledown), $S^* = 3.2$ (\blacksquare), $S^* = 4.5$ (\circ), $S^* = 5.1$ (\triangle), and $S^* = 6.1$ (\triangledown).
.....55

Figure 3.19. Normalized time duration of the Nusselt number increment at the vertical position where the temporal-local heat transfer coefficient is maximized at the centerline ($y = y_{max}^*$; $x = 0$).
.....56

Figure 3.20. Integral value of the increased normalized Nusselt number ($Nu^* - 1$) over the whole normalized time.57

Figure 3.21. Nusselt number profile (\bullet) where the heat transfer enhancement is maximized ($x = 0$, $y = y_{max}^*$, and $z = 0$), and wall-directional velocity profile (\blacktriangle) near the wall ($x = 0$, $y = y_{max}^*$, and $z = 0.2d_{eq}$): $S^* = 1.5$ (a), $S^* = 2.4$ (b), and $S^* = 3.2$ (c), of which the

cases where the Nusselt number increases again in the middle of decline. Domains corresponding to the green-dotted box on the time axis are magnified, which is plotted on the upper-right part.....58

Figure 3.22. Nusselt number profile (●) where the heat transfer enhancement is maximized ($x = 0$, $y = y_{max}^*$, and $z = 0$), and wall-directional velocity profile (▲) near the wall ($x = 0$, $y = y_{max}^*$, and $z = 0.2d_{eq}$): $S^* = 0.5$ (a), $S^* = 4.5$ (b), $S^* = 5.1$ (c), and $S^* = 6.1$ (d), of which the cases where the Nusselt number decreases gradually after the enhancement. Domains corresponding to the green-dotted box on the time axis are magnified, which is plotted on the upper-right part.....59

Figure 3.23. The maximum horizontal normalized Nusselt number at $y = y_{max}^*$: $S^* = 0.5$ (●), $S^* = 1.5$ (▲), $S^* = 2.4$ (▼), $S^* = 3.2$ (■), $S^* = 4.5$ (◆), $S^* = 5.1$ (○), and $S^* = 6.1$ (△).....60

Figure 3.24. Temporal normalized spanwise vorticity (ω_x^*) field (a), and timely synchronized and normalized Nusselt number (Nu^*) field (b), which are timely synchronized, when bubble-wall distance (S^*) is 0.5 (bubble-wall collision; linearly-rising bubble). Here, a helps to describe normalized spanwise vorticity contour level and length of the unit vector, t^* denotes the normalized time, and y_b^* means the normalized vertical location of the bubble.....61

Figure 3.25. Dimensionless velocity distribution for various Prandtl numbers, which is reported by Ostrach, 1952.....62

Figure 3.26. Dimensionless temperature distribution for various Prandtl numbers, which is reported by Ostrach, 1952.....63

Figure 3.27. Normalized vertical velocity (v^*) profile along the normalized wall-normal direction (z^*): of the zigzag-rising bubble (a); of the linearly-rising bubble (b). Red solid line shows the location of z^* where the vertical velocity is zeros, which denotes the thickness of the momentum thermal boundary layer.....64

Figure 3.28. Vertical profile of the normalized Nusselt number when the spherical bubble periodically bounces (a) and when the spherical bubble initially bounces (b). The symbol denoted by the red arrow is the position where the temporal-local Nusselt number is maximized, and red number means the corresponding normalized Nusselt number.
.....65

Figure 3.29. Temporal normalized spanwise vorticity (ω_x^*) field (a), and timely synchronized and normalized Nusselt number (Nu^*) field (b), which are timely synchronized, when bubble-wall distance (S^*) is 0.5 (no heat transfer; linearly-rising bubble). Here, a helps to describe normalized spanwise vorticity contour level and length of the unit vector, t^* denotes the normalized time, and y_b^* means the normalized vertical location of the bubble.....66

Chapter 1

Introduction

The dynamics of the heat transfer enhancement by the bubble has been investigated for a long time, because of their scholarly and practical importance. In boiling, not only the generation of the bubble due to the phase change is the main mechanism of the heat transfer, but also the forced convection by the bubble detachment and movement plays an importance role in heat transfer growth. Additionally, the effect of the bubble is the important factor in many industrial fields like internal combustion engine block cooling, pressurized water nuclear reactors and heat exchanger (Delaure et al., 2003; Jung and Kim, 2014).

Deen and Kuipers, 2013 numerically made a situation that the bubble of 10 *mm* initial diameter rose near the heated vertical wall, and they found out that the heat transfer was enhanced evidently in the vicinity of the bubble, whereas relatively low heat transfer was observed at the below of the bubble because of the local thermal saturation. Additionally, they discovered that the heat transfer was increased considerably when the bubble collided with the vertical wall. Scammell and Kim, 2015 conducted an experiment with a Taylor vapor bubble. They figured out that the main heat transfer contributor was turbulent mixing in the bubble wake. Also, they discovered that the amount of heat transfer enhancement was declined when the background fluid velocity was increased due to the decreased bubble residence time over a certain location of the tube. Fershtman et al., 2016 investigated local instantaneous heat transfer enhanced by two

consecutive rising bubbles in slug flow, and they found out that temporal cooling effect was strongly affiliated with the momentum transfer rate specified by the local fluid dynamics. Donoghue et al., 2014 measured the change of the convective heat transfer when the rising bubble ($d_{eq} \sim 3.37$ mm; $Re \sim 1453$) impinged under the horizontal heated plate, where d_{eq} and Re denote equivalent diameter and Reynolds number of the bubble, respectively. Depending on the bubble impacting location, they defined four specific locations: edge, center, front and rear part of the bubble. Among them, the maximum heat transfer increment occurred at the rear part, where the cooling rate rose up to 22 times higher. In the other locations, however, heat transfer rate soared up to about 10 times when the initial collision occurred and grew again when the bubble bounced. Although quantitative flow velocity field was not visualized, they analogized the flow velocity based on the bubble velocity and shape, and explained the heat transfer enhancement mechanisms. When a bubble ($d_{eq} \sim 4.75 - 9.14$ mm) slides under 30° inclined febrific surface, Donnelly et al., 2015 observed the bubble dynamics and the local heat transfer coefficient. They discovered that when the initial temperature of the plate was raised, the shape of a bubble fluctuated, because the surface tension and viscosity of the fluid were reduced. Also, sliding speed of the bubble was increased due to the increased flow speed in the convective boundary layer and decreased drag coefficient. Heat transfer coefficient was increased at the wake region of the bubble, and it was increased locally up to eight times higher and globally up to twice times higher compared with the natural convection. As time goes by, the local heat transfer rate returned to the original state, and the cooling region got broaden.

When the size of the bubble became bigger, the intensity of the heat transfer was stronger because of the higher advection speed and stronger vortex shedding. Meehan et al., 2017 investigated the bubble-wake interaction of two in-lined sliding bubbles ($d_{eq} \sim 5.8\text{ mm}$; separation distance $\sim 3-7d_{eq}$) under 30° inclined heated plate. They found that when the trailing bubble entered in the wake of the leading bubble, the trailing bubble was accelerated, which implies that there was interaction between the wake of the leading bubble and the trailing bubble. Local convective heat flux increased up to eight times higher than that of the natural convection, and presence of trailing bubble helped to rise the heat transfer. However, in some local spots, the trailing bubble could impede local-temporal cooling rate, because the trailing bubble could take away the cool fluid induced by the leading bubble wake. Thus, they found out that heat transfer enhancement was not only a function of the mixing by the wake of the bubble but also the interaction between the bubble and the wake. Hollingsworth et al., 2009 investigated the cooling effect of the sliding vapor bubble in 27°C FC-87 fluid, of which boiling point is 30°C at 1 atm , and they found out that the heat transfer coefficient was a function of the fluid velocity, fluid property, surface boundary condition and initial temperature field. Delaure et al., 2003 measured the bubble induced forced convection on rectangular surface of which angle was modifiable, and they visualized flow field near the plate with particle image velocimetry (PIV). They found that the inclined plate could influence on the bubble dynamics and the growth heat transfer rate, and they suggested that two heat transfer mechanisms. First, change of flow velocity near the wall varies the convective heat flux, and second, fluctuation of near-wall fluid temperature changes

the cooling rate. However, detailed measurement of bubble dynamics was not performed, as the contrast between the bubble image and the background image was not clear. Changing the volume of bubble and passing it closely to the vertical wall, Kumar et al., 1992 estimated the enhancement of heat transfer coefficient of the heated vertical surface. The increment was larger when the size of the bubble is bigger, and they found out that when the bubble–wall distance was further, it needed more time to obtain the instantaneous maximum heat transfer, which was due to the wake shedding time. Although they visualized the flow field with the polyolite particle, quantitative study of velocity field with digital particle image velocimetry (DPIV) (Willert and Gharib, 1991) was not conducted.

Forced convection on the heated wall is strongly coupled with the bubble dynamics and the bubble induced flow. Therefore, for investigating the heat transfer mechanisms, analysis of the bubble dynamics and the flow field is important. Lee and Park, 2017 studied the bubble dynamics and the motion of wake structure of a zigzagging bubble ($d_{eq} \sim 2.35$ mm; $Re \sim 750$; $We \sim 3.3$; $Eo \sim 0.75$), where We and Eo means Weber number and Eötvös number, respectively. Using shadow image technique (SIT), they measured the size, aspect ratio and velocity of a bubble, and they also visualized the wake structure with vorticity contour, using PIV. Also, with changing the distance between a rising bubble and the vertical wall, they investigated the interaction between the wall and the vorticity behind of a bubble, and they modeled the vertical motion of vortex structure. Jeong and Park, 2015 measured the rising motion of near-wall zigzagging bubble ($d_{eq} \sim 3.92$ mm; $Re \sim 1100$; $We \sim 4.4$; $Eo \sim 2.1$), and they found out that the presence of the wall effects on the bubble properties:

amplitude of the motion, periodicity, rising velocity, wavelength and aspect ratio of a bubble. They also accounted the shape and path of a bubble in terms of momentum and energy gain/loss of a bubble.

Additionally, it is well known that the shape and path of the bubble are a function of the bubble size, Reynolds number and Weber number. Haberman and Morton, 1953 suggested that a bubble of $Re < 400$ was spherical and a bubble of $400 < Re < 5000$ was ellipsoidal. Also, Duineveld, 1995 proposed characteristics of two kinds of the bubble path: straight ($Re < 662$; $We < 3.3$; $d_{eq} < 1.82$ mm) and zigzag ($Re > 662$; $We > 3.3$; $d_{eq} > 1.82$ mm).

In present study, with high-speed camera, we will observe the shape of the bubble using SIT, and will visualize the flow field with PIV. Moreover, using infrared camera (IR camera), we will measure the instantaneous wall temperature field, which is timely and spatially synchronized with the high-speed camera. By this means, we will measure the quantitative convective heat transfer increment as a two-dimensional field, and will establish the mechanisms of heat transfer enhancement based on the vortex shedding motion and flow velocity near the heated vertical wall.

Chapter 2

Experimental set-up and procedure

2.1. Single bubble rising near a vertical wall

The present study is conducted in $300 \times 130 \times 280\text{ mm}$ water tank containing 15°C tap water (Figure 2.1(a)). A needle is installed at 25 mm height from the floor, and gently pushed by a syringe pump (Fusion 100 Touch, Revodix Inc.). It is well known that a bubble generally rises in straight, helical and zigzag path, depending on the Reynold number, Weber number, diameter and aspect ratio of a bubble (Haberman and Morton, 1954; Hartanian and Sears, 1957; Aybers and Tapucu, 1969; Duineveld, 1994). Moreover, we experimentally observe that a bubble takes different trajectory depending on the water temperature or shape of the nozzle tip, even if the size of a bubble is identical. In our experiment, the bubble is made through a needle which has a sharp tip in the 15°C tap water, and by changing the size of needle inner diameter, we vary the size of the bubble. Commonly, inner diameter of a needle is standardized through a unit called gauge (G). We test with the 22, 23 and 24 G needle, which has an inner diameter of 0.41, 0.34 and 0.31 mm , respectively. 22G needle makes 2.8 mm zigzagging bubble, 23 G needle makes 2 mm bubble which firstly moves linearly and changes to helical path, and 24 G needle makes 1.1 mm straight rising bubble. Therefore, in our experimental set-up, the linear movement of the bubble gradually becomes unstable between the bubble diameter of $1.1 - 2.0\text{ mm}$, and the bubble trajectory changes to zigzagging path

between the bubble diameter of 2.0 – 2.8 mm. We focus on the linearly rising bubble and the zigzagging bubble, using 22 and 24 G needle. Time interval of each bubbles is about 30 seconds, which is enough to dissipate the effect of the previous bubble. When it is zigzagging bubble, shape of the bubble is ellipsoidal of which the aspect ratio (χ) is $\chi = d_{maj}/d_{min} = 2.0 (\pm 0.09)$, and the equivalent diameter (d_{eq}) is $d_{eq} = (d_{maj}^2 d_{min})^{1/3} = 2.8 (\pm 0.1) \text{ mm}$, which is calculated from the two dimensional bubble image, where d_{maj} and d_{min} are length of the major and minor axis of the bubble (Figure 2.1(d)). When it is zigzagging bubble, terminal rising velocity (\bar{U}_b) is $\bar{U}_b = 0.29 \text{ m/s}$ and Reynolds number (Re) is $Re = \bar{U}_b d_{eq} \nu^{-1} = 750$. Moreover, Weber number (We) is $We = \rho_l \bar{U}_b d_{eq} \sigma^{-1} = 3.2$, and Eötvös number (Eo) is $Eo = g(\rho_l - \rho_g) d_{eq}^2 \sigma^{-1} = 1.19$, (ν is the kinematic viscosity, ρ_l and ρ_g are the density of the water and air, and σ is surface tension of the water). On the other hand, when it is linear bubble, spherical bubble ($\chi = 1.1$) of 1.1 mm (d_{eq}) rises at the speed of 0.22 m/s (\bar{U}_b), of which non-dimensional properties are $Re = 220$, $We = 0.77$ and $Eo = 0.16$. Shapes and trajectories of both kinds of bubble are in good agreement with previous studies (Haberman and Morton, 1953; Duineveld, 1995).

Coordinate systems of x , y , and z -axis mean transvers, vertical, and wall-normal directions, respectively (Figure 2.1(a)), which are normalized as $x^* = x/d_{eq}$, $y^* = y/d_{eq}$, and $z^* = z/d_{eq}$, respectively. Also, normalized x , y and z -directional velocities are expressed as $u^* = u/\bar{U}_b$, $v^* = v/\bar{U}_b$ and $w^* = w/\bar{U}_b$, respectively. When the bubble approaches the wall closest, we set this point as vertical directional origin point (Figure 2.1(c)). However, when it is the linear bubble, without any collision, vertical directional origin point is set as center

position of the field of view. Each of transvers and wall-normal directional origin point is located on a bubble center and on the wall (Figure 2.1(c)). The minimum distance (S_{min}) between the vertical wall and the bubble center is normalized with d_{eq} ($S^* = S_{min}/d_{eq}$) (Figure 2.1(d)). When it is zigzagging bubble, S^* is varied $S^*=0.5, 1.5, 2.4, 3.2, 4.5, 5.1, 6.1$ and 9.7 . In the case of $S^*=0.5$, the bubble collides with the wall, but in the other cases, the bubble passes by the wall adjacently. On the other hand, when it is the linear bubble, S^* is $S^*=0.5$ and 3.7 , where the bubble impacts and does not impact on the wall, respectively.

2.2. High-speed two-phase particle image velocimetry

To observe the shape and motion of the gas phase, and to measure liquid velocity field induced by a passing bubble simultaneously, we use a high-speed two-phase particle image velocimetry (Lindken and Merzkirch, 2002).

In order to conduct high-speed two-phase PIV, we use a high-speed camera (SpeedSense M310, Dantec Dynamics) to capture the images of gas and liquid phase (resolution of $1280 \times 800 \text{ px}$ with 500 Hz). For separating the gas phase out of captured image, we illuminate LED (red-colored, wavelength of 675 nm), which can penetrate only the liquid phase, from the back of a bubble. Therefore, the bubble is represented as a black lump on the image (Figure 2.1(c)), and this process is called shadow image technique (SIT). To visualize the motion of the liquid phase, continuous-wave (CW) laser (RayPower 5000, Dantec Dynamics) is used to make a green laser

sheet (wavelength of 532 nm) which illuminates the PIV seeding particles (PMMA Rhodamine-B, size ranging 1–20 μm) that absorbs 560 nm and emit 584 nm wavelength. Particle Stokes number (St_p), defined as the ratio of the particle response time (τ_p) to the fluid response time (τ_f), is calculated as

$$St_p = \frac{\tau_p}{\tau_f} = (\rho_p d_p^2 / 18 \mu_p) / (d_{eq} / \bar{U}_b) \approx 7.3 \times 10^{-4}$$

which means the particles will not affect on the fluid motion.

To get the bubble and particle image, 105 mm macro lens (Nikon) is used, and orange filter (cut-off length of ~ 570 nm, Heliopan) is equipped for screening the green laser reflected from the bubble. Therefore, the only red color light from the LED and fluorescent seeding particle can be captured on the camera. Moreover, as the intensity of the LED and the fluorescent light is different, we can distinguish the particle from LED background image (Figure 2.1(c)). Images of seeding particles are analyzed by cross-correlation using fast Fourier transform algorithm (interrogation window of 32 x 32 px and 75 % overlap). Spatial interval of each vectors is 8 px, which is 0.21–0.36 mm (0.08 – 0.2 d_{eq}). At the same, from the binarized bubble images, we calculate the size, shape and velocity of a bubble, using a particle tracking velocimetry (PTV) algorithm. More details of the high-speed two-phase PIV are mentioned in Lee and Park, 2017.

2.3. Convective heat transfer flux measurement

At the one side of the chamber, we equip 300 x 100 mm foil (Goodfellow, AISI 316 25 μm foil), to which spatially constant

electric heat flux (q_{gen}) is provided ($q_{gen} = IV/A = 2100 \text{ W/m}^2$) with a power supply (GEN6-200 DC power supply, LAMBDA), where I and V mean current and voltage indicated on power supply gauge, and A denotes the area of the foil, and the temperature of the foil is 17–20°C. On the outer side of the stainless foil, we aid 21 μm matt black paint (emissivity of 0.95), for preventing the flection of infrared (IR) rays and for calculating the radiation heat transfer ($q_{rad} = \varepsilon \sigma T^4$), where ε , σ and T is emissivity, Stefan–Boltzmann constant and local temperature of the foil, respectively. When the local heat transfer is maximum, Biot number of the foil (Bi_f) and of the paint (Bi_p) are calculated as $Bi_f \approx 7.3 \times 10^{-3}$ and $Bi_p \approx 176 \times 10^{-3}$. In front of the painted side of the foil, germanium IR-glass (8–12 μm AR coated, Edmund optics) is located, making thin entrapped air gap. Therefore, convective heat transfer toward the outer environment can be assumed as the conduction with the medium of the thin air gap, and we measure the amount of conductive heat transfer (q_{cond}) by locating thermocouple at the 3 mm distance from the foil ($q_{cond} = -k_{air} \partial T / \partial z$, k_{air} is the thermal conductivity of the air which is 26 kW/m K) (Figure 2.1(b)). Heat is also transferred and stored in the wall itself, which is called lateral heat conduction $q_{lateral}$ and heat storage q_{cap} , which is represented as Eq. (1) and Eq. (2), respectively, and properties of the foil and paint are noted on Table 2.1. IR camera (A655sc LWIR camera, FLIR) captures the temperature field of the foil (resolution of 240 x 640 px with 100 Hz) which is timely synchronized with high-speed camera by a function generator (Timing hub XS-TH, IDT Vision). For increasing the accuracy of the IR camera, we have adjusted the temperature of the IR camera to the temperature of the black body

(GBR400, Gilwoo) of which temperature accuracy is $\pm 0.4 K$. Figure 2.2 shows the temperature difference of the black body and the IR camera, over the black body temperature of $287 - 294 K$. The maximum temperature difference is about $0.3 K$, which is about 0.1% of the black body temperature. Therefore, the IR camera is calibrated well, and we concluded that the accuracy of the IR camera is $\pm 0.7 K$.

Before calculating the convective heat flux q''_{conv} , temperature field is smoothed with Gaussian filter. Then, temperature field is converted into energy flux by being applied into energy balance equation, Eq. (3), where q''_{laser} denotes the laser energy absorbed in the foil, and detailed consideration of q''_{laser} will be treat in the section 2.4. (Donoghue et al., 2014; Donnelly et al., 2015; Meehan et al., 2017)

$$q''_{lateral} = - \left(k_f \delta_f + k_p \delta_p \right) \left(\frac{\partial^2 T}{\partial x^2} + \frac{\partial^2 T}{\partial y^2} \right). \quad (1)$$

$$q''_{cap} = \left(\rho_f C_p f \delta_f + \rho_p C_p p \delta_p \right) \frac{\partial T}{\partial t}. \quad (2)$$

$$q''_{conv} = q''_{gen} - q''_{cond} - q''_{rad} - q''_{lateral} - q''_{cap} + q''_{laser}. \quad (3)$$

Our experimental height is $130 - 220 mm$ where the Rayleigh number is lower than 10^9 , which means thermal boundary layer is laminar. In this location, the effect of the wall induced turbulence is small, and it is suitable to analyze the effect of the bubble induced turbulence (Incropera et al., 2007).

2.4. Laser energy absorbed in the foil (q''_{laser})

For conducting PIV, we inevitably project the laser sheet on the foil which absorbs the laser energy, and it must be considered in

energy balance equation of Eq. (3). However, it is very difficult to measure the absorbed laser energy (q^{laser}), because spread laser has spatially varying intensity, and also determining the ratio of the absorption to the refection of the light on the foil surface is difficult. However, considering that the laser intensity profile and absorption ratio do not change over time, we can solve the energy balance equation without measuring the q^{laser} .

Sequence of data are over regularly spaced intervals of 0.01 s, as the IR-camera operates in 100 Hz, and we express N^{th} convective heat flux equation as Eq. (4), where N subscript denotes N^{th} equation.

$$q^{\text{conv},N} = q^{\text{gen}} - q^{\text{cond},N} - q^{\text{rad},N} - q^{\text{lateral},N} - q^{\text{cap},N} + q^{\text{laser}} \dots \quad (4)$$

Here, we subtract the first equation ($N = 1$) from the n^{th} equation ($N = n$). Then, as the q^{gen} and q^{laser} are eliminated, n^{th} convective heat flux ($q^{\text{conv},n}$) is represented with one unknown variable of $q^{\text{conv},1}$ and the measurable variables of q^{cond} , q^{rad} , q^{lateral} , and q^{cap} . Therefore, if we can specify the $q^{\text{conv},1}$, we can calculate the $q^{\text{conv},n}$.

The first convective heat transfer flux ($q^{\text{conv},1}$) is natural convection, without any effect of the bubble. So, we stop the syringe pump and wait until the natural convective heat flux is saturated. Then, we suddenly screen the laser and immediately measure the reference convective heat transfer flux ($q^{\text{conv,ref}}$), which is possible using Eq. (3) because q^{laser} is zero. As the amount of convective heat transfer should change sequentially over time, we can assume that $q^{\text{conv},1}$ is same with $q^{\text{conv,ref}}$. In this way, we can calculate every convective heat flux (q^{conv}), without measuring absorption of

laser energy (q_{laser}).

2.5. Uncertainty

When calculating the bubble properties, defocus errors can be caused, because the location of the bubble center may be at the out of focused plane. Therefore, evaluation of the bubble characteristics from the changeable image magnification factor can yield uncertainties (Bongiovanni et. al., 1997). In present study, uncertainties in bubble properties of diameter, aspect ratio and velocity are 3.37 %, 2.59 % and 1.47 %, respectively, depending on the threshold of binarization process.

Measuring fluid velocities also has an uncertainty depending on various factors, which is described by Lawson et. al., 1999. In Eq. (5), δ denotes the percentage error, u_{piv} is measured fluid velocity, M is the magnification factor, Δs is the particle displacement, and Δt is the time separation.

$$\delta(u_{piv}) = \sqrt{\delta(M)^2 + \delta(\Delta s)^2 + \delta(\Delta t)^2} \quad (5)$$

In our study, the percentage error of magnification factor $\delta(M)$ is 0.4 – 0.9 % with M is 26 – 45 $\mu m/px$. The particle displacement error (Δs) is calculated by the pixel resolution divided by the mean particle movement. As the pixel resolution is 0.1 pixel, $\delta(\Delta s)$ is 1.1 %. Finally, for the time separation error (Δt), the high-speed camera operating at 500 Hz has an error of 0.025 %. Therefore, the percentage error of fluid velocity calculated from PIV ($\delta(u_{piv})$) is 1.2 – 1.4 %.

In Eq. (3), the q_{conv} is the function of measured variables which

have their own uncertainties. Based on the error propagation analysis, uncertainty of the function of Eq. (6) is noted on Eq. (7): X and Y are the variables of function q , and δX , δY and δq denotes the uncertainties of X , Y and q (Clifford, 1973).

$$q=q(X, Y, \dots) \quad (6)$$

$$\delta q = \sqrt{\left(\frac{\partial q}{\partial X} \cdot \delta X\right)^2 + \left(\frac{\partial q}{\partial Y} \cdot \delta Y\right)^2 + \dots} \quad (7)$$

The resulting uncertainty of convective heat flux is 5 – 20 %, and the maximum uncertainty is when the convective heat flux is highest, due to the increased uncertainty of lateral heat transfer flux term and heat storage flux term, which is corresponding with the previous studies (Donoghue et. al., 2014; Donnelly et. al., 2015; Meehan et. al., 2017).

Foil	Thermal conductivity k_f	16.3 W/m K
	Thickness δ_f	$25 \mu\text{m}$
	Density ρ_f	7960 kg/m^3
	Specific heat C_{Pf}	502 J/kg K
Paint	Thermal conductivity k_p	0.57 W/m K
	Thickness δ_p	$21 \mu\text{m}$
	Density ρ_p	1162 kg/m^3
	Specific heat C_{Pp}	2835 J/kg K

Table 2.1. Properties of the foil and the paint.

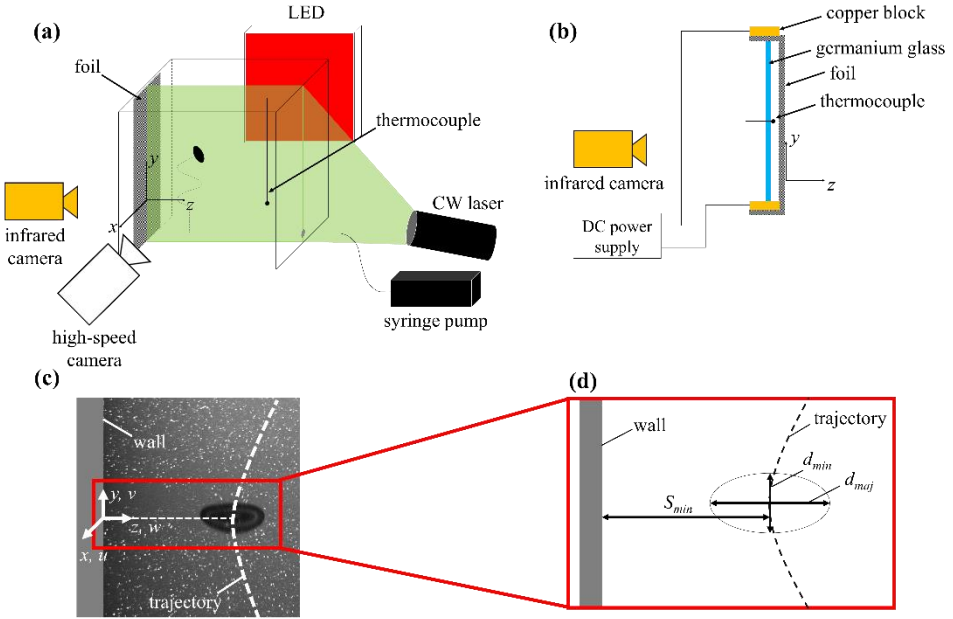


Figure 2.1. (a) Experimental setup for observing the flow velocity field at ($y - z$) plane and for measuring the temperature field of the foil at ($x - y$) plane, using high-speed two-phase particle image velocimetry and infrared camera. (b) Power supplying system for heating the foil, and measurement systems of the wall temperature field and air-gap temperature. (c) Raw image of the high-speed camera in ($y - z$) plane, when a bubble passes the summit point of the path ($t = 0$). (d) Magnified schematic diagram for defining the bubble information.

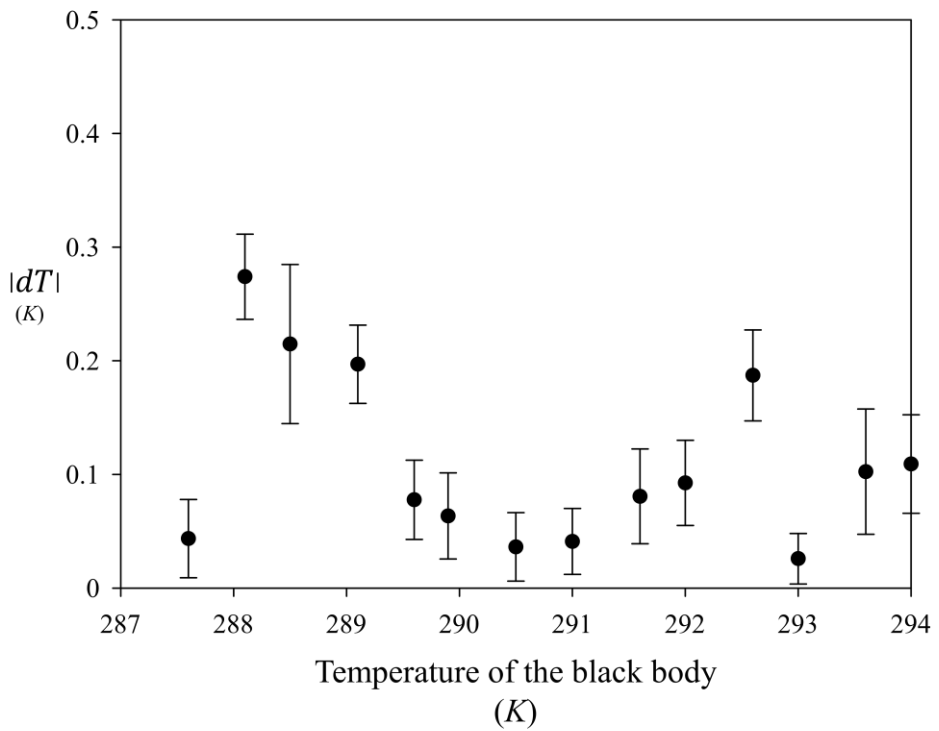


Figure 2.2. Temperature difference between the infrared camera and the black body, as a function of the black body temperature.

Chapter 3

Results and discussion

3.1. Zigzagging bubble – global Nusselt number

Lee and Park, 2017 visualized the wake of a zigzagging bubble, and observed the vortex structures emanated around the summit point of the trajectory, where vortexes are developed and finally detached. They reported that vortex structures keep their movement with the same convective velocity just for a short time after the pinch-off. However, based on their modeling equation, the convective velocity of the vortex structures finally decreases, and the vortex motion is eventually dissipated. Therefore, for understanding the bubble induced wall convective heat transfer, we have to study about the wake motion and its strength. We extract the vortex boundary with the 0.1 threshold of normalized spanwise vorticity ($(\omega_x^* = \omega_x d_{eq} \bar{U}_b^{-1} = 0.1)$), and then based on the vortex boundary we calculate the center of the vortex structures (Figure 3.1). Trace of the vortex structures and corresponding flow speed are represented in Figure 3.2. We observe the maximum intensity of normalized wall-normal velocity inside of the vortex boundary and use it as a represent strength of the vortex structure, as it is the most effective flow motion for cooling the heated wall, which will be explained in later part. Four vortex structures are traced because only they can reach to the wall when the normalized bubble-wall distance ((S^*)) is close enough. Among them, the vortex structure, which mostly tends

to move laterally, is denoted as a circular symbol, and others are represented with triangle, square and inverted triangle, respectively (Figure 3.2(a)). Vortex structures, which finally convect to the wall, are marked in Figure 3.2(b–h). However, when it is the case that no forced heat transfer occurs ($S^*=9.7$), we trace every four vortex structures (Figure 3.2(i)). After the wake pinch off, every vortexes maintains their inertia and spreads to the upper-lateral direction (Ellingsen and Risso, 2001). When the vortex reaches the wall, it quickly dissipates with upward movement. From the Figure 3.2, it can be inferred that the number of the point, where heat transfer is enhanced, would be varied depending on the normalized bubble-wall distance (S^*). Also, when the bubble is further from the wall, it needs more time to increase the heat transfer after the bubble passes the summit point, because the vortex needs the time to reach the wall. Furthermore, because the intensity of the vortex gradually weaken, wall-cooling rate would get smaller, as the normalized bubble-wall distance (S^*) is larger. We will now verify the previous inference through the temperature field of the wall.

To understand the overall phenomenon, the instantaneous normalized spanwise vorticity (ω_x^*) contour and normalized Nusselt number contour of the wall, which are timely synchronized, are plotted in Figure 3.3 – Figure 3.10. Here, time (t) is normalized by the bubble period (T): $t^* = t/T$, and we define the reference time ($t^* = 0$) as the moment when the bubble passes the summit point of its trajectory. Also y_b^* denotes the normalized vertical position of a bubble, and because of the vortex dissipation, the graphs at each time have different contour level and different length of unit vector, which is expressed by a variable “ a ”. In Figure 3.3, for S^* of 0.5, a bubble

rises most closely to the wall with a strong wall effect (Lee and Park, 2017). Nusselt number starts to increase when a bubble begins to touch the wall ($t^* = -0.1$), and then as a bubble bounces, local Nusselt number is gradually enhanced and maximized ($t^* = 0.1$). By this time, the Nusselt number is increased explosively at a single spot, because the bubble entrains bulk liquid to the wall as it collides. However, as the time goes by ($t^* = 0.1 - 0.3$), single peak of the Nusselt number is divided into two peaks. The reason can be explained in the normalized vorticity field at $t^* = 0.3$. Bouncing off from the wall, the bubble leaves a vortex structure on the wall, which locally disturbs the recovery of thermal boundary layer. This phenomena was also reported by de Vries et al., 2002 that vorticity accumulated behind the bubble is shed near the wall as the bubble impinges on the wall. To sum up, as a bubble comes to the wall, it directly draws bulk liquid, and when the bubble bounces off, it leaves an eddy which renews the local surface fluid. At $t^* = 10$, vortexes are almost dissipated, but heat transfer is still enhanced, which perhaps the entrained liquid is not warmed yet. Additionally, the Nusselt number is gradually weakened and cooling area moves upward, which might be due to the flow in the convective boundary layer (Incropera et al., 2007). In Figure 3.4, a bubble rises adjacently to the wall ($S^* = 1.5$) with small wall effect (Lee and Park, 2017). At $t^* = 0.4 - 0.6$, vortex structures are shed behind a bubble and convect to the wall, which finally reach the wall and enhance the wall–heat transfer coefficient. After the vortex touches the wall, vorticity decreases exponentially, but normalized Nusselt number keeps increasing ($t^* = 0.4 - 0.6$). Later, the other vortex structures arrive the wall, and they make the other peaks of forced convective spot ($t^* = 0.1; t^* = 1.8$), which is marked

with the red arrow in Figure 3.4(b). As the time goes by ($t^* = 11$), each of the peaks are united and changed to one broad peak, and also heat transfer enhanced area moves upward. In Figure 3.5 ($S^* = 2.4$), bubble moves almost freely, because of the research reported by Lee and Park, 2017 that when $S^* = 1.9$, the bubble is little affected by the wall. Like the case of $S^* = 1.5$, eddies spread to the wall ($t^* = 0 - 1$) and locally enhance the wall heat transfer coefficient. Because each of the vortex structures arrives the wall sequentially, wall–convective heat transfer spots, which is indicated with red arrows, are made in order, and forced convection finally occurs at four locations ($t^* = 5.3$). In Figure 3.6, a bubble passes near the wall with $S^* = 3.2$. After a bubble passes the summit point of the trajectory, vortexes are induced behind the bubble and they shift toward the wall ($t^* = 0 - 1.5$). At $t^* = 1.5$, one vortex reaches the wall and local Nusselt number starts to increase at one spot. While the vortex is being dissipated, the Nusselt number keeps increasing and is maximized at $t^* = 2.6$, but still, only one vortex is interacting with the wall and other vortexes could not reach the wall yet. Other eddies arrive the wall later and weakly enhance the local heat transfer, which make three peaks of normalized Nusselt number ($t^* = 6.0$). As the time elapses, increment of heat transfer is decreased and its area moves upward, and the boundaries of the three peaks of increased Nusselt number are being disappeared. In Figure 3.7, where normalized bubble–wall distance (S^*) is 4.5, four vortexes convect to the wall, but only two vortexes can arrive the wall before the dissipation. Therefore, local heat transfer enhancement occurs at two spots, and they move upwards over time ($t^* = 23$). In Figure 3.8 and Figure 3.9, where S^* is 5.1 and 6.1, only one vortex entrains bulk

liquid to the wall, and heat transfer increment arises at one spot. Like previous cases, although vorticities are totally disappeared, the Nusselt number is still increased compared to the initial state. In Figure 3.10, where S^* is the largest. there is no heat transfer enhancement, because every vortexes is dissipated before they arrive at the wall. To sum it up, when there are bubble–wall impaction ($S^* = 0.5$, Figure 3.3), a bubble directly drags surrounding liquid to the wall, and the interaction between the wall and the bubble creates a vortex attached to the wall. Therefore, there is strong local heat transfer enhancement, eight time higher compared to the initial state, and forced convection occurs at two spots. However, when a bubble passes without direct interruption of the wall, the bubble make several vortex structures which convect to the wall. Some of them reach the wall and locally increase the heat transfer coefficient. Each vortexes has different tendency to move laterally. Therefore, as the S^* gets further, the number of the normalized Nusselt number peaks decreases. Also, among the vortexes, one eddy, which prone to moving laterally, is the most efficient at rising heat transfer coefficient. Additionally, there are some common phenomenon in all cases: forced convective area moves upward, because of momentum convective boundary layer (Incropera et al., 2007), and heat transfer coefficient is still higher than the initial state, although the vortex is already dissipated. This may be because the cold water entrained by the bubble wake needs time to warm up. If we use the laser–induced–fluorescence (LIF) which helps to observe the temperature field of the liquid phase, more detailed mechanisms of heat transfer can be established.

Figure 3.11 shows the timely consecutive vertical directional

normalized Nusselt number (Nu^*) contour as a function of normalized time (t^*), at the centerline ($x^* = 0$, which is marked as white dashed line in Figure 3.3(b) – Figure 3.10(b)). As mentioned previously, when the bubble rises closely to the wall ($S^* = 1.5$; $S^* = 2.4$), heat transfer coefficient is increased at four points. However, as the distance between the wall and the bubble (S^*) gets further, the number of the position, where the heat transfer is enhanced, decreases, and finally between $S^* = 6.1$ and $S^* = 9.7$, the cooling effect on the wall disappears: two large peaks ($S^* = 0.5$), four peaks ($S^* = 1.5$; $S^* = 2.7$), three peaks ($S^* = 3.2$), two peaks ($S^* = 4.5$), one peak ($S^* = 5.1$; $S^* = 6.1$) and no heat transfer increment ($S^* = 9.7$). Lee and Park, 2017 reported that if the normalized bubble–wall distance (S^*) is 1.9, wall gives a small effect on a bubble, however we find that a bubble can affects on the wall at much more further distance. When the bubble collides with the wall (Figure 3.11(a)), heat transfer enhancement occurs almost immediately ($t^* \sim 0$). On the other hand, when the bubble passes the wall without impingement (Figure 3.11(b)–(g)), there is a noticeable time delay until heat transfer is enhanced after the bubble passes the summit point. This is because when a bubble impacts on the wall, bubble entrains the surrounding cold fluid directly on the surface, but otherwise eddies, made near the bubble path, move to the wall over time, and that is why the time delay becomes longer as the normalized bubble–wall distance (S^*) gets larger. After the normalized local Nusselt number is maximized, intensity of the Nusselt number decreases, and vertical affected area moves upwards, which was explained previously.

In Figure 3.12, upper and lower boundary where the Nusselt number is increased and average normalized Nusselt number in

affected area are plotted as a function of normalized time (t^*). Average temporal normalized Nusselt number tends to decrease as S^* becomes larger, which is same trend with the instantaneous normalized local Nusselt number. Nusselt number enhancement starts at a small spot, and then affected area gets broad over time. This is firstly because eddies emanated behind the bubble reach the wall sequentially (Figure 3.2), and secondly because of the vertical directional diffusion. Figure 3.13 shows vertical width (Δy^*), where the normalized Nusselt number is increased, as a function of normalized time (t^*). When it is the case where the four Nusselt number peaks are created ($S^* = 1.5$; $S^* = 2.7$), vertical width of heat transfer enhancement (Δy^*) is largest. However when there are three and two Nusselt number peaks ($S^* = 3.2$; $S^* = 4.5$, respectively) there are not noticeable difference in Δy^* , and then as the S^* becomes more further, Δy^* tends to decrease. Although the case of $S^* = 0.5$ has only two forced convective spots, strong wall-normal velocity and advection induced by a direct impingement of a bubble help to enhance heat transfer over broad range. In conclusion, if the normalized bubble-wall distance (S^*) is smaller, the Nusselt number tends to increase over wide vertical range, except for the case of $S^* = 0.5$.

Wall-directional vortex boundary, which is set by the threshold of $\omega_x^* = 0.1$ (Figure 3.1(b)), is traced, and in Figure 3.14, measured normalized time when the end of the vortex touches the wall is plotted as a blue-triangle symbol. When the normalized bubble-wall distance (S^*) is 4.5, 5.1 and 6.1, normalized spanwise vortex boundary of 0.1 ($\omega_x^* = 0.1$) disappears before it touches the wall, so we extrapolate the position of the vortex and predict the vortex-wall

impacting time. Also, on Figure 3.14, the normalized times when the Nusselt number starts to increase (t^*_{ini}) and when the Nusselt number becomes maximized (t^*_{max}) are marked. As expected, the moment of the vortex–wall impingement and the time of the initial heat transfer enhancement (t^*_{ini}) are in good agreement. Moreover, the initial Nusset number rising time (t^*_{ini}) and the Nusselt number maximized time (t^*_{max}) increase exponentially as a function of S^* . Lee and Park (2017) reported that the vertical speed of vortex, possibly related to the wall–normal motion, developed behind the ellipsoidal zigzagging bubble decays exponentially. Their finding implies that when the S^* gets larger, the time to interact between the vortex and the wall increases exponentially, which corresponds with our finding. Considering that the time difference between t^*_{ini} and t^*_{max} gets larger over S^* (Figure 3.14), and enhancement of the instantaneous local normalized Nusselt number decreases as S^* gets larger, we catch that the time gradient of Nusselt number becomes smaller as S^* increases. Therefore, the time gradient of normalized Nusselt number from t^*_{ini} to t^*_{max} : $\delta(Nu^*)/\delta(t^*)$ is shown in Figure 3.15, and we find that the time gradient of the Nusselt number decreases exponentially as the normalized distance (S^*) becomes longer.

For comparing the temporal variation of the local Nusselt number with the flow induced near the wall, fluid motion at $0.2d_{eq}$ away from the wall ($z^*=0.2$; $x^*=0$) is analyzed, because the interrogation window of the PIV vector, which is too close to the wall, includes the wall and this can cause unexpected error. At the centerline of x –axis ($x^*=0$) and $0.2d_{eq}$ away from the wall in z –axis ($z^*=0.2$), vertical (y –directional) variation of the normalized wall–normal velocity, vertical velocity and vorticity are extracted. Then, the maximum absolute

values of each normalized flow components ($|w^*|$; $|v^*|$; $|\omega_x^*|$), and the maximum normalized Nusselt number (Nu_{max}^*) are plotted on Figure 3.16, as a function of S^* . When the bubble impacts on the vertical wall ($S^* = 0.5$), intensity of the convective heat transfer is raised up to about eight times higher. In all cases, as like before, the physical quantities tends to decrease exponentially over the S^* . Ellingsen and Risso, 2001 reported that the maximum velocity behind the ellipsoidal bubble decays exponentially over time. Therefore, when the distance between the wall and a bubble (S^*) gets further, the degree of thermal boundary layer disturbance caused by the flow induced in the wall is weakened exponentially, and that is why the maximum normalized Nusselt number is decreased over S^* . For comparing the correlation degrees of the maximum temporal-local normalized Nusselt number and the maximum instantaneous-local normalized absolute values of each flow component ($|w^*|$; $|v^*|$; $|\omega_x^*|$), we use two values: Pearson correlation coefficient (ρ) and p -value, which is shown on Table 3.1. ρ is a value between -1 and 1 . Here, if we verify the relationship between X and Y , $\rho = -1$ or $\rho = 1$ denotes that X and Y are in perfect negative or positive correlation, respectively, and $\rho = 0$ means X and Y have no relationship. p -value is used to test the null hypothesis which is generally rejected when the p -value is less than significance level of 0.05 . (Gibbons and Chakraborti, 2003; Curran-Everett and Benos, 2004) Three flow components of the maximum normalized wall-normal velocity, vertical velocity and vorticity correlate well with the maximum normalized Nusselt number because p -value is significantly smaller than 0.05 and ρ is close to one. Among them, Pearson correlation coefficient (ρ) between the maximum

temporal-local normalized wall-normal velocity ($|w^*|$) and the maximum instantaneous-local normalized Nusselt number ($|Nu^*|$) is largest, which means that the amount of heat transfer increment is mostly affected by the wall-normal velocity strength.

In Figure 3.17, the normalized vertical position where the instantaneous local Nusselt number is maximum (y_{max}^*) and the normalized vertical location at which strength of each temporal-local flow components ($|w^*|$; $|v^*|$; $|\omega_x^*|$) is maximized are marked. As S^* increases, y_{max}^* is shifted upward exponentially. With the y_{max}^* , which is marked as red-circular symbol in Figure 3.17, vertical position, where the normalized temporal intensity of the local wall-normal velocity ($|w^*|$) is maximized, matches mostly. Reminding that the maximum temporal-local normalized Nusselt number correlates best with the strength of maximum instantaneous-local normalized wall-normal velocity, we conclude that the wall-normal velocity is the most effective flow component for enhancing the convective heat transfer. According to Kumar et al., 1992 there are two mechanisms of forced convection when a bubble passes near the vertical heated wall: firstly shear flow in the wake makes the thermal boundary layer thin and secondly vortex entrains the surrounding cool fluid and renews the hot liquid near the surface. According to the results of our study, which discovers that wall-normal velocity is more effective than vertical velocity for cooling vertical heated wall, surface renewal is more dominant mechanism than shear flow induced thinned thermal boundary layer.

Ellingsen and Risso, 2001 discovered that the maximum fluid velocity, which is induced by zigzagging-ellipsoidal bubble, tends to decrease exponentially, and also, Lee and Park, 2017 reported that

vertical speed of the vortex induced by the zigzagging–ellipsoidal bubble decreases exponentially. Our study is consistent with previous studies in that the cooling effect of a bubble changes exponentially as S^* is changed. Moreover, we find that the time when the Nusselt number starts to increase after the bubble passes the summit point, time gradient of Nusselt number and vertical position where the local–Nusselt number is maximized (y_{max}^*) are varied exponentially over S^* . Additionally, we observe that the wall–normal velocity is mostly effective to enhance the wall–convective heat transfer than other flow components. Also, more detailed analysis will be done at the normalized vertical position where the instantaneous local Nusselt number is maximized (y_{max}^*).

3.2. Zigzagging bubble – local Nusselt number at y_{max}^*

Now, let us discuss about the variation of the local Nusselt number at y_{max}^* , where the temporal heat transfer coefficient is maximized. In Figure 3.18, temporal variations of the normalized Nusselt number at y_{max}^* are marked as a function of normalized time. As mentioned in previous part, it is obvious that the maximum increment of the Nusselt number is decreased as S^* becomes larger. Also after the bubble passes the summit point of the trajectory ($t^* = 0$), the elapsed time until the Nusselt number initially increases gets longer over S^* . Moreover, it is clearly observed that when the normalized Nusselt number firstly increases and decreases, the slop of the normalized Nusselt number over normalized time becomes gradual at bigger S^* . In every cases, enhanced Nusselt number goes back to the initial

state when the normalized time is about 30, and more detailed analysis about a time duration of the forced convection ($Nu^* > 1.1$) at y_{max}^* is denoted in Figure 3.19. In previous, most data (maximum normalized Nusselt number; normalized time when the Nusselt number starts to increase or become maximized; time gradient of the normalized Nusselt number; vertical position where the normalized Nusselt number is maximized) is varied gradually over S^* . However, time duration of increased heat transfer coefficient (Δt^*) is higher when there is moderate bubble–wall distance. The time duration of forced convection is longest when the bubble rises with moderate distance from the wall ($S^* = 2.4$; $S^* = 3.2$), which implies that the amount of heat transfer accumulated over time can be larger when a bubble passes at some distance from the wall. Therefore, increased normalized Nusselt number ($Nu^* - 1$) is integrated over the normalized time, which corresponds to the bottom dimensions of each plots in Figure 3.18 with the base of the $Nu^* = 1$, and it is denoted in Figure 3.20. Like the time duration of the forced heat transfer (Δt^*), the accumulated Nusselt number ($\int (Nu^* - 1) dt^*$) is higher when there is proper bubble–wall distance. In previous part, it is observed that the instantaneous heat transfer is effectively enhanced when the distance between the wall and the bubble is short ($S^* = 0.5$). However, it is found that it is effective for accumulated heat transfer when the distance between the wall and the bubble is rather long ($S^* = 2.4$; $S^* = 4.5$). The accumulated increment of the normalized Nusselt number, which tends to be maximized at a moderate size of S^* , decreases suddenly at $S^* = 3.2$. Comparing the variation of Nu^* over t^* in Figure 3.18, we find the reasons. For the case of $S^* = 2.4$ and $S^* = 3.2$, first increment of Nu^* is similar, but the amount of secondly

enhanced Nu^* is much larger for $S^* = 2.4$, of which reason will be followed. Based on Figure 3.2, circular-symbol vortex makes the maximum instantaneous-local Nusselt number, of which position is defined as y_{max}^* , and invert-triangle-symbol vortex entrains bulk liquid underneath y_{max}^* , which moves upward with exchanging heat with the wall. Because two vortexes (\bullet ; ∇) gradually recede with each other as they moves, if the distance between the wall and the bubble is greater, the two locations where the bulk liquid is induced will be farther away, which means that the liquid induced below need to move more distance to reach the y_{max}^* and it implies that the liquid is more warmed. In summary, when S^* is farther, because the liquid induced at lower position exchanges heat for longer time to reach the y_{max}^* , the second Nusselt number increment is get small. For the case of $S^* = 3.2$ and $S^* = 4.5$ in Figure 3.18, amount of maximum Nu^* is similar, but increasing and decreasing rate is different. Compared to the cased of $S^* = 3.2$, as the vortex of $S^* = 4.5$ approaches more slowly to the wall and more slowly moves along the wall, the rate of Nusselt number change over time is smaller, resulting in a larger amount of heat transfer at y_{max}^* for the entire time. Also, studying about why the total amount of heat transfer is small for the case of small S^* , we speculate that too fast flow velocity induced on the wall may dissipates or moves away quickly, which shortens the time for perturbing the thermal boundary layer. Therefore, we plot Figure 3.21 and Figure 3.22, and they show the normalized Nusselt number over the normalized time at y_{max}^* with the wall-directional normalized flow velocity ($-w^*$) which is induced in front of the wall ($y = y_{max}^*$; $z = 0,2d_{eq}$). In every cases, the normalized Nusselt number increases by the wake of the bubble and then goes back to the initial state

(Figure 3.18). However, in some cases, normalized Nusselt number is enhanced again during decay ($S^* = 1.5$; $S^* = 2.4$; $S^* = 3.2$). It is because the vortex, which is marked as circular symbol in Figure 3.2, creates the location where the maximum heat transfer occurs (y_{max}^*), and underneath it another vortex, which is denoted as inverted triangle in Figure 3.2, draws cold liquid into the wall which moves upwards, and it provokes additional heat transfer at y_{max}^* . Figure 3.21 shows the normalized Nusselt number and wall-directional flow velocity over the normalized time, where the Nusselt number increases again while it decreases, and small graph in each plots denotes the magnified graph in specific time, which is marked as dotted-green box in t^* -axis. As we inferred above, wall-directional velocity ($-w^*$) tends to decrease quickly when S^* is shorter. Also, there is trend that the time when the flow velocity near the wall grows and the moment when the Nusselt number increases is different. We interpret this phenomenon as follow. Because flow velocity is measured by $32 \times 32 \text{ px}$ interrogation window and the center of the interrogation window is located at $0.2d_{eq}$ from the wall, flow velocity can be measured in the interrogation window before the entrained bulk liquid actually touches the wall. Also, warm water in the thermal boundary layer, which may be initially induced to the wall, is not that effective in enhancing heat transfer. Therefore, heat transfer variation may react later than the measured flow velocity induced on the wall. Moreover, the rapid decrease in flow velocity induced in the wall means that the flow is interacting with the wall, and that is why the normalized Nusselt number begins to increase when the intensity of wall-normal velocity starts to decrease. During the overall time, the normalized Nusselt number is enhanced sharply

first, and then starts to decrease as the wall–directional flow near the wall is totally dissipated. However, the trend of decreasing Nusselt number stops and it increases slightly. Mechanisms of the two kinds of forced convection (first–sharp increase; second–slight increase) is different: first enhancement is due to the direct liquid entrainment from the surrounding, and second growth is because the cold liquid induced below rises upward. In Figure 3.22, variation of the normalized Nusselt number at y^*_{max} and wall–directional flow velocity near the wall ($y = y^*_{max}$; $z = 0.2d_{eq}$) are shown as a function of S^* . However, in this cases ($S^* = 0.5$; $S^* = 4.5$; $S^* = 5.1$; $S^* = 6.1$), normalized Nusselt number consistently decreases after the first increment. Again, the normalized Nusselt number tends to increase as the wall–directional flow rate decreases. However, in the case of $S^* = 0.5$, as the bubble directly renews the heated surface and then leave the vortex, the time when flow is induced and the moment when heat transfer is enhanced are similar.

Until now, we mainly focused on the Nusselt number profiles in vertical direction (y –directional), and we defined the vertical position, where the instantaneous–local heat transfer is maximized, as y^*_{max} . From now on, horizontal (x –directional) normalized Nusselt number will be studied at $y = y^*_{max}$ (Figure 3.23). At the centerline ($x^* = 0$) which corresponds to the zigzagging plane of the bubble, normalized Nusselt number is maximized (actually, peak position is slightly shifted from $x^* = 0$, but it is a limitation of a manual experiment), and centered on $x^* = 0$, the Nusselt number has a Gaussian distribution. Additionally, ellipsoidal–zigzagging bubble enhances heat transfer over a range about three times of the bubble size ($-1.5d_{eq} - 1.5d_{eq}$) in the horizontal (x) direction. Lee and Park,

2017 visualized the liquid velocity field of the ellipsoidal–zigzagging bubble in x – z plane. Based on their figure, vortex emanated behind the zigzagging bubble can range from $-1 d_{eq}$ to $1 d_{eq}$ at least, and from $-2 d_{eq}$ to $2 d_{eq}$ at large, which supports our result about horizontal affected area.

3.3. Straight bubble

When it is the ellipsoidal–freely rising bubble, which moves in the zigzagging path, vortex structures created behind the bubble moves to the lateral direction and disturbs the thermal boundary layer of the wall. Also, when the ellipsoidal bubble impacts on the wall, bubble entrains bulk liquid to the wall and then leave a strong vortex which renews the surface fluid. Therefore, zigzag–rising bubble is very efficient for cooling the heated vertical wall (the maximum instantaneous–local heat transfer coefficient rises up to eight times higher), though amount of heat transfer increment is different depending on the bubble–wall distance. de Vries, 2001 visualized the wake of a linearly rising small bubble ($d_{eq} < 1.4 \text{ mm}$) using a two–way Schlieren system, and observed that the single threaded wake is formed at the rear part of a bubble and it does not spread from the bubble path, which means linearly rising small bubble may be not efficient for enhancing the wall–convective heat transfer. Therefore, we analyze the forced convective heat transfer effect of a small straightly rising bubble ($d_{eq} = 1.1 \text{ mm}$) with changing the distance from the wall: $S^* = 0.5$ (bubble–wall impingement) and $S^* = 3.7$ (bubble freely rises). When the vertical wall is heated, upward flow

is induced near the wall, because of the lowered density of heated liquid. Therefore, if the position where a bubble is firstly injected is close enough, it is attracted toward the wall by the lift force and collides with the wall. When a bubble impinges on the wall, the normalized distance between the bubble and the wall (S^*) is 0.5. Figure 3.24 shows the temporal normalized flow field and timely matched normalized Nusselt number contour of the linearly-rising small bubble which impinges on the wall ($S^* = 0.5$). Compared to the case where the zigzag-rising bubble impacts on the wall, vorticity shed from the linearly-rising small bubble is much smaller. Moreover, as the wavelength of the bubble-trajectory is much larger than the amplitude of the collision cycle, vertical velocity is dominantly induced on the wall with small intensity of the wall-normal velocity. When the bubble bounces on the wall ($t^*=0$), heat transfer coefficient is not varied, but as the bubble passes by ($t^*= 0.7$; $t^*= 1.7$), wake behind the bubble is left on the wall, which slightly enhances convective heat transfer. Although we do not visualize the thermal boundary layer, it is possible to indirectly calculate the approximate thickness of the thermal boundary layer by measuring the thickness of the momentum boundary layer. Figure 3.25 and Figure 3.26 show the “dimensionless velocity distributions for various Prandtl numbers” and “dimensionless temperature distributions for various Prandtl numbers”, respectively, which is reported by Ostrach, 1952. Here, Gr , T , T_∞ and T_s mean the Grashof number, liquid temperature, bulk liquid temperature and wall-temperature, respectively. The wall-normal position (z) where the liquid vertical velocity (v) is zero is the momentum boundary layer thickness, and the wall-normal location (z) where the liquid temperature (T) is same with the T_∞ is

the thermal boundary layer thickness, which are defined as z_m and z_t . Our research is conducted in the 15°C water, which has the Prandtl number of 8.2, and as represented in Figure 3.25 and Figure 3.26, the ratio of z_t to z_m is roughly less than half. This means that the thermal boundary layer thickness is thinner than half of the momentum boundary layer thickness. Figure 3.27 shows the averaged-normalized vertical directional velocity profile: zigzagging bubble (a); linearly-rising bubble (b). Finding the z-position where the normalized velocity is zero, we get to know that the momentum boundary layer thickness of the zigzagging bubble and the linearly-rising bubble is $2.8d_{eq}$ and $7.1d_{eq}$, respectively. Therefore, the thickness of the thermal boundary layers of each cases are roughly calculated: $<1.4d_{eq}$ (zigzagging bubble) and $<3.6d_{eq}$ (straight bubble). In Figure 3.3 – Figure 3.10, z-directional size of the vortex structures emanated from the zigzagging bubble are comparable with the thermal boundary layer thickness ($<1.4d_{eq}$). Therefore, they effectively mix hot fluid on the surface and cold bulk liquid. However, when it is a linearly-rising small bubble, the z-directional area affected by the wake of a bubble is evidently smaller than the thickness of the thermal boundary layer ($<3.6d_{eq}$). So the exchange between hot and cold liquid does not occur actively, which is one of the reasons why straight-rising small bubble is not efficient for heat exchange. In Figure 3.28, the normalized Nusselt number of a straight-rising small bubble, which firstly impacts on the wall, is analyzed however, it is not visibly different from the heat transfer effect of the periodically impacting small bubble.

Figure 3.29 shows the instantaneous normalized flow field and timely synchronized normalized Nusselt number contour of the linearly-

rising small bubble which rises freely without any impaction ($S^* = 3.7$). Single thread wake is created behind the bubble, but it does not convect to the lateral direction and cannot entrains the bulk liquid to the heated wall. Therefore, heat transfer coefficient by a straight-rising small bubble is negligible.

	Nu^* & $ w^* $	Nu^* & $ v^* $	Nu^* & $ w^* $
ρ	0.87	0.84	0.77
$P - \text{value}$	8.39×10^{-40}	4.84×10^{-35}	1.59×10^{-25}

Table 3.1. Pearson correlation coefficient (ρ) and p -value between normalized maximum Nusselt number (Nu^*) and normalized maximum absolute value of wall normal velocity ($|w^*|$), vertical velocity ($|v^*|$) and vorticity ($|\omega_x^*|$) induced near the wall ($0.2d_{eq}$ from the wall) at zigzagging plane ($x = 0$).

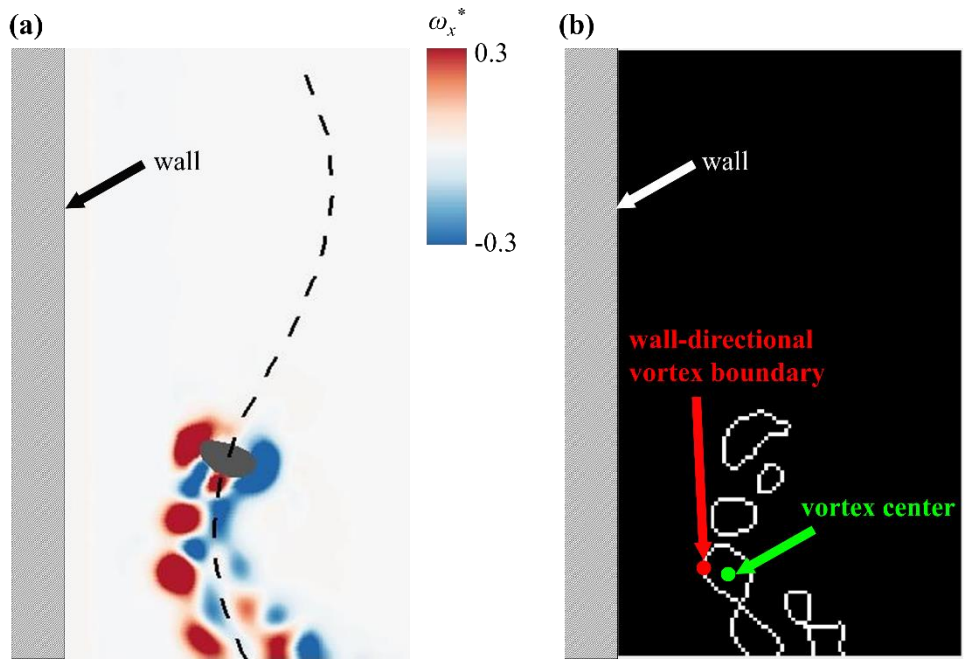


Figure 3.1. (a) Normalized vorticity (ω_x^*) contour image. (b) Boundary of the vortex set by the threshold of $\omega_x^* = 0.1$.

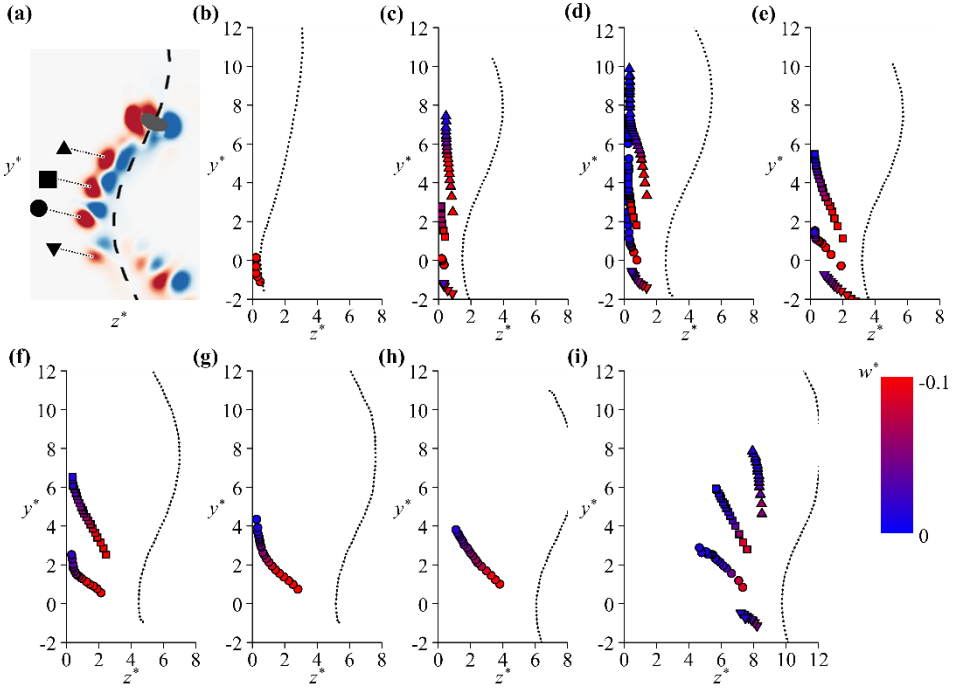


Figure 3.2. Position of the vortex structures: created near the summit point (●), first below the summit point (▼), first and second above the summit point (■ and ▲, respectively) (a), and bubble trajectory (•••): $S^* = 0.5$ (b), $S^* = 1.5$ (c), $S^* = 2.4$ (d), $S^* = 3.2$ (e), $S^* = 4.5$ (f), $S^* = 5.1$ (g), $S^* = 6.1$ (h), and $S^* = 9.7$ (i). In (b–i), the color contour denotes the normalized wall normal velocity.

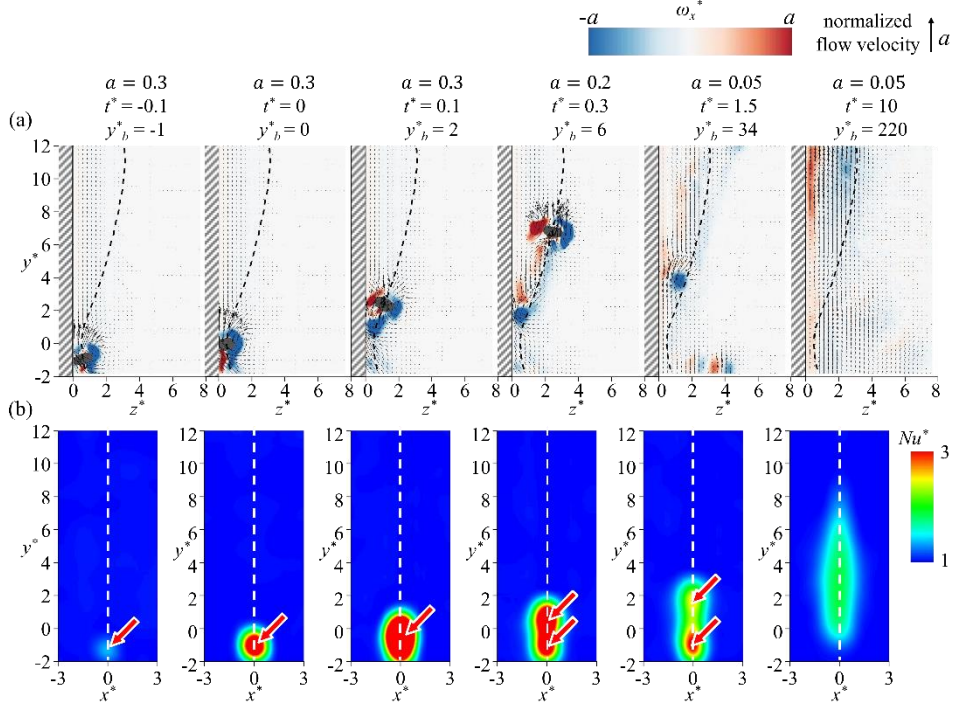


Figure 3.3. Temporal normalized spanwise vorticity (ω_x^*) field (a), and timely synchronized and normalized Nusselt number (Nu^*) field (b), which are timely synchronized, when bubble–wall distance (S^*) is 0.5 (bubble–wall collision ; zigzag–rising bubble). Here, α helps to describe normalized spanwise vorticity contour level and length of the unit vector, t^* denotes the normalized time, and y_b^* means the normalized vertical location of the bubble.

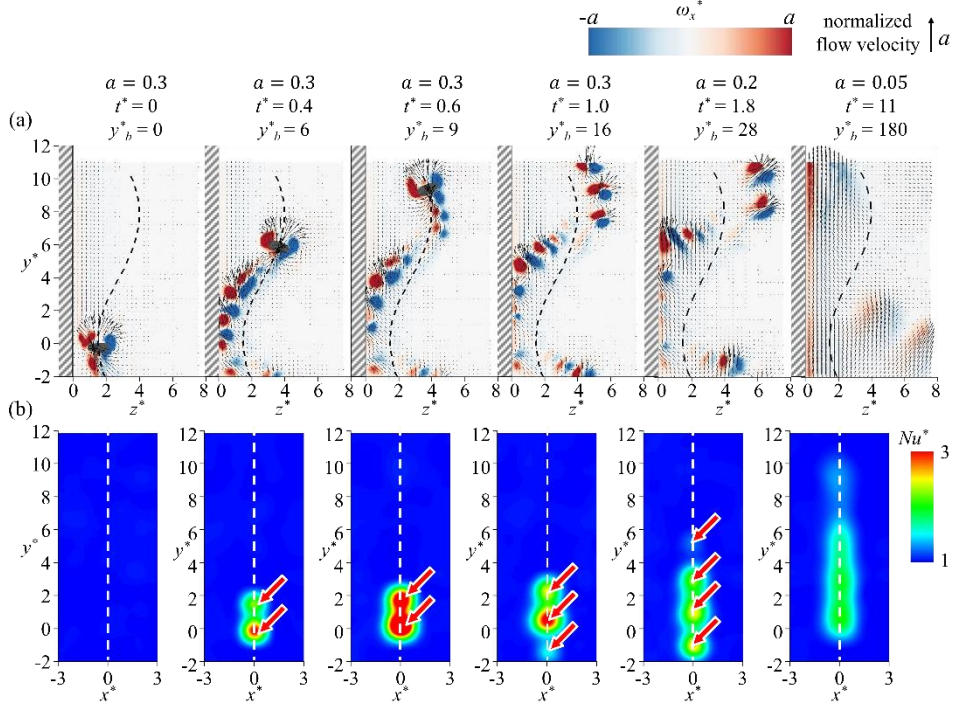


Figure 3.4. Temporal normalized spanwise vorticity (ω_x^*) field (a), and timely synchronized and normalized Nusselt number (Nu^*) field (b), which are timely synchronized, when bubble–wall distance (S^*) is 1.5 (bubble passes near the wall; zigzag–rising bubble). Here, a helps to describe normalized spanwise vorticity contour level and length of the unit vector, t^* denotes the normalized time, and y_b^* means the normalized vertical location of the bubble.

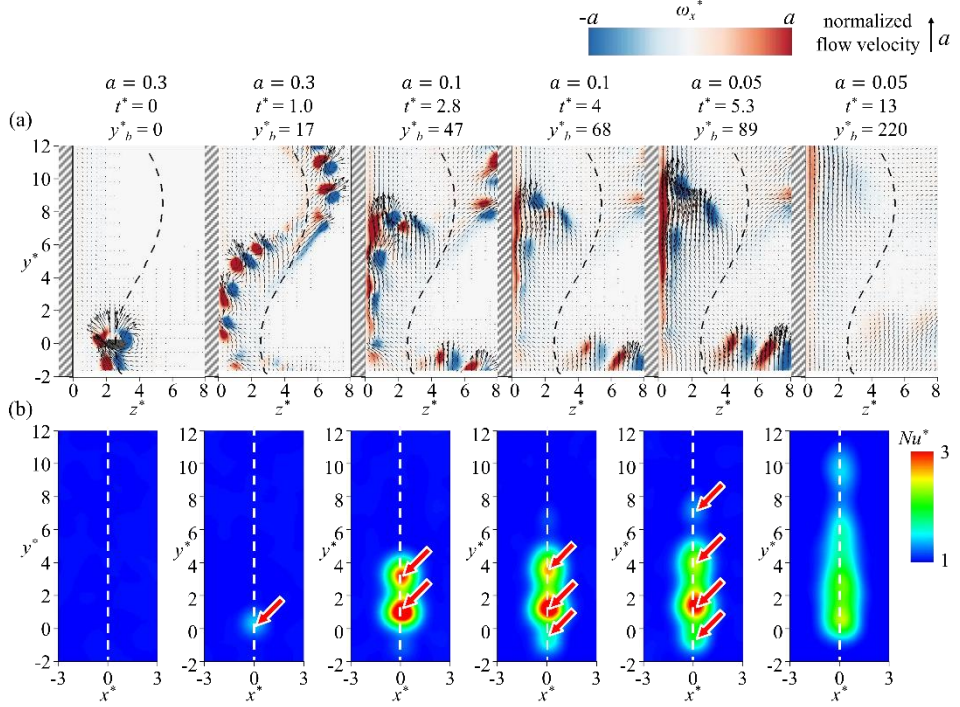


Figure 3.5. Temporal normalized spanwise vorticity (ω_x^*) field (a), and timely synchronized and normalized Nusselt number (Nu^*) field (b), which are timely synchronized, when bubble–wall distance (S^*) is 2.4 (bubble passes near the wall; zigzag–rising bubble). Here, α helps to describe normalized spanwise vorticity contour level and length of the unit vector, t^* denotes the normalized time, and y_b^* means the normalized vertical location of the bubble.

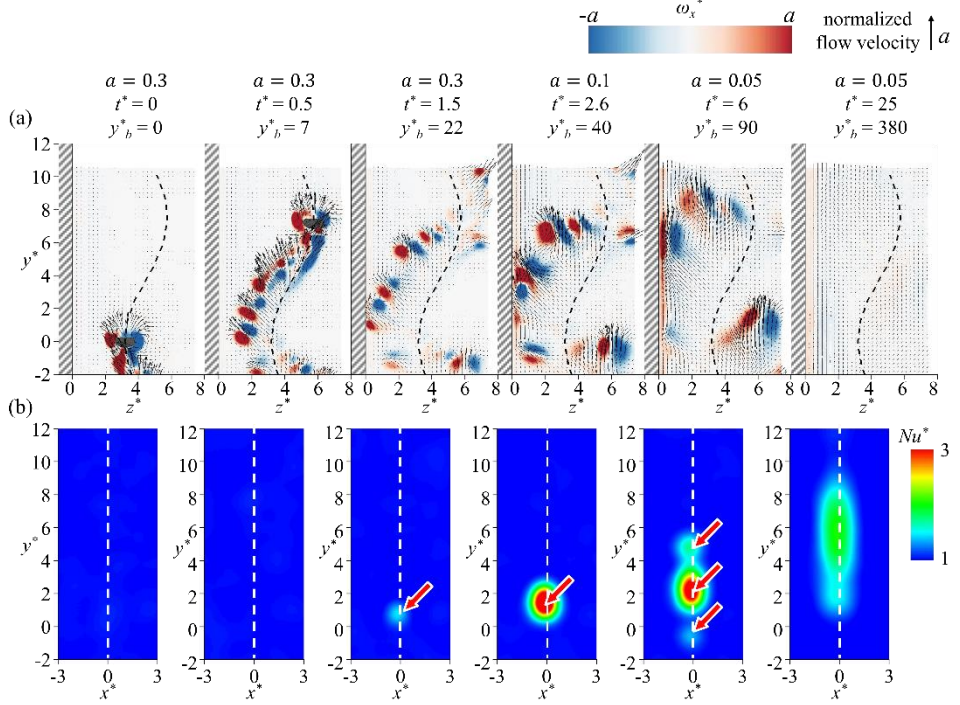


Figure 3.6. Temporal normalized spanwise vorticity (ω_x^*) field (a), and timely synchronized and normalized Nusselt number (Nu^*) field (b), which are timely synchronized, when bubble–wall distance (S^*) is 3.2 (bubble passes near the wall; zigzag–rising bubble). Here, α helps to describe normalized spanwise vorticity contour level and length of the unit vector, t^* denotes the normalized time, and y_b^* means the normalized vertical location of the bubble.

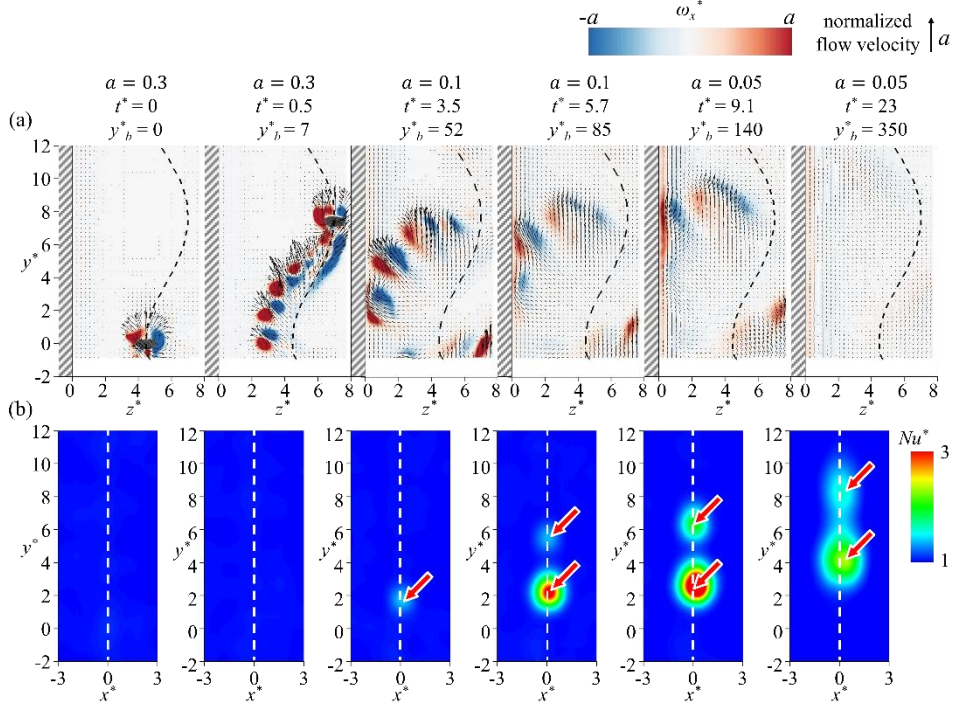


Figure 3.7. Temporal normalized spanwise vorticity (ω_x^*) field (a), and timely synchronized and normalized Nusselt number (Nu^*) field (b), which are timely synchronized, when bubble–wall distance (S^*) is 4.5 (bubble passes near the wall; zigzag–rising bubble). Here, a helps to describe normalized spanwise vorticity contour level and length of the unit vector, t^* denotes the normalized time, and y_b^* means the normalized vertical location of the bubble.

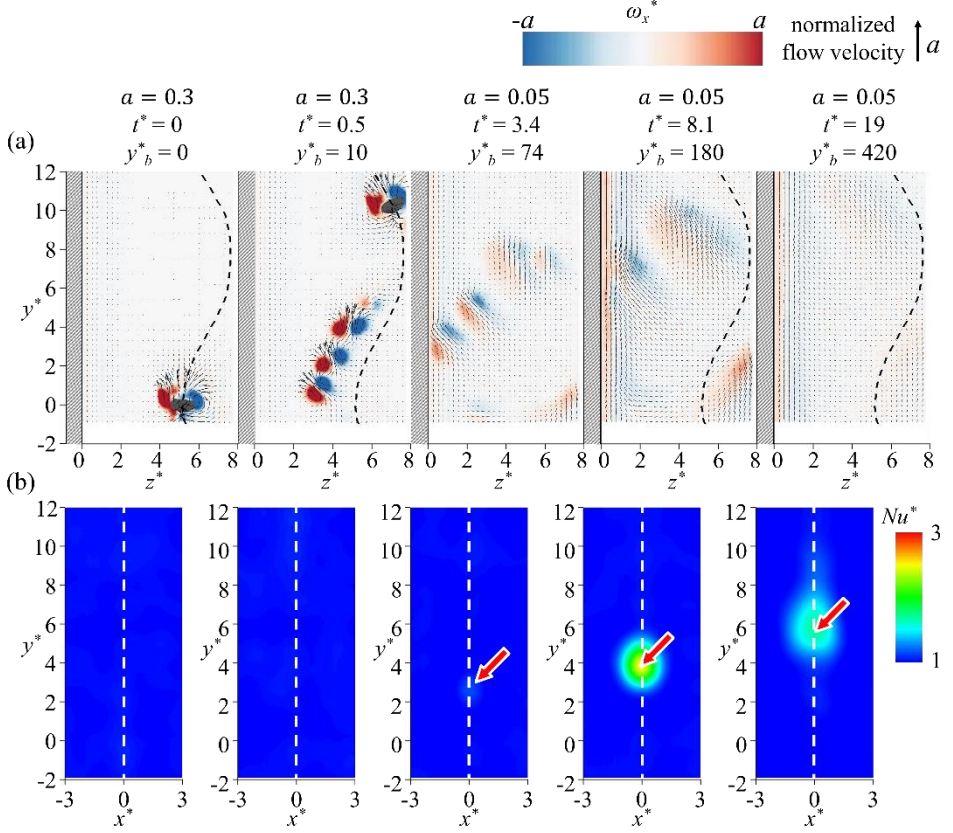


Figure 3.8. Temporal normalized spanwise vorticity (ω_x^*) field (a), and timely synchronized and normalized Nusselt number (Nu^*) field (b), which are timely synchronized, when bubble–wall distance (S^*) is 5.1 (bubble passes near the wall; zigzag–rising bubble). Here, a helps to describe normalized spanwise vorticity contour level and length of the unit vector, t^* denotes the normalized time, and y_b^* means the normalized vertical location of the bubble.

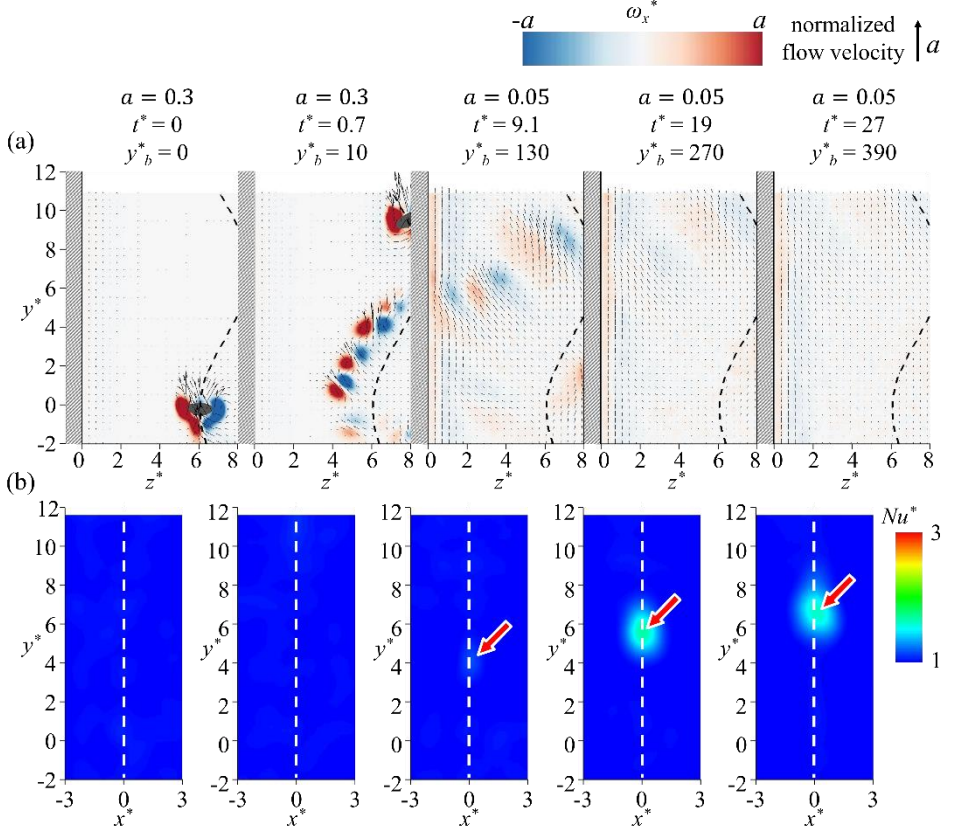


Figure 3.9. Temporal normalized spanwise vorticity (ω_x^*) field (a), and timely synchronized and normalized Nusselt number (Nu^*) field (b), which are timely synchronized, when bubble–wall distance (S^*) is 6.1 (bubble passes near the wall; zigzag–rising bubble). Here, a helps to describe normalized spanwise vorticity contour level and length of the unit vector, t^* denotes the normalized time, and y_b^* means the normalized vertical location of the bubble.

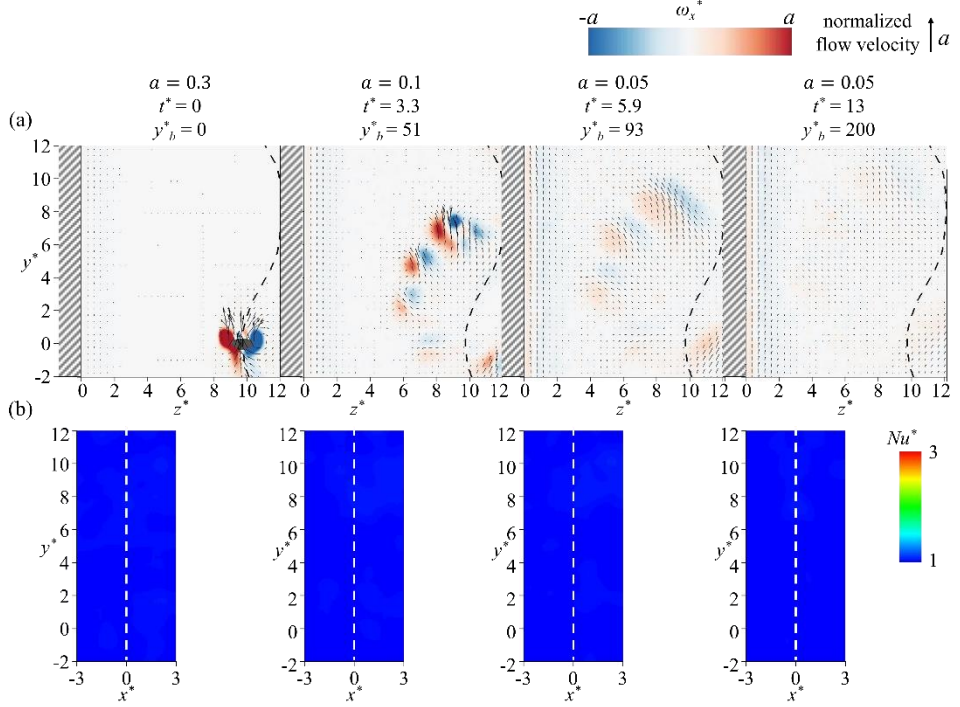


Figure 3.10. Temporal normalized spanwise vorticity (ω_x^*) field (a), and timely synchronized and normalized Nusselt number (Nu^*) field (b), which are timely synchronized, when bubble–wall distance (S^*) is 9.7 (no heat transfer; zigzag–rising bubble). Here, a helps to describe normalized spanwise vorticity contour level and length of the unit vector, t^* denotes the normalized time, and y^*_b means the normalized vertical location of the bubble.

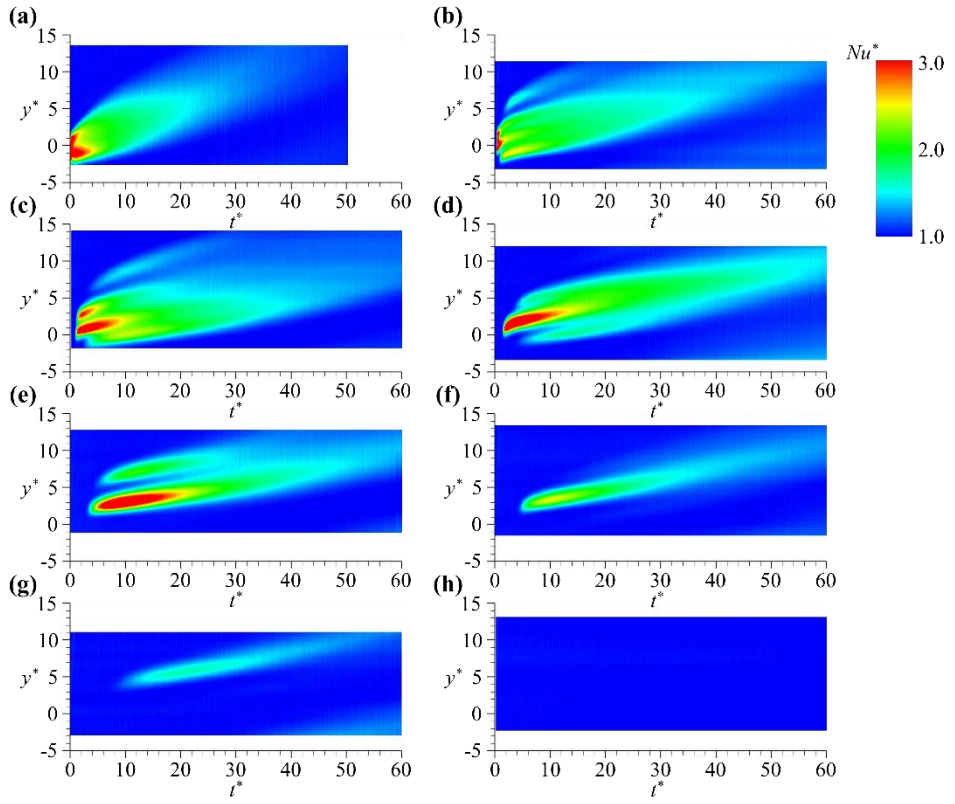


Figure 3.11. Temporal variation of the one-dimensional (at $x = 0$, and $z = 0$) normalized Nusselt number (Nu^*) contour: $S^* = 0.5$ (a), $S^* = 1.5$ (b), $S^* = 2.4$ (c), $S^* = 3.2$ (d), $S^* = 4.5$ (e), $S^* = 5.1$ (f), $S^* = 6.1$ (g), and $S^* = 9.7$ (h).

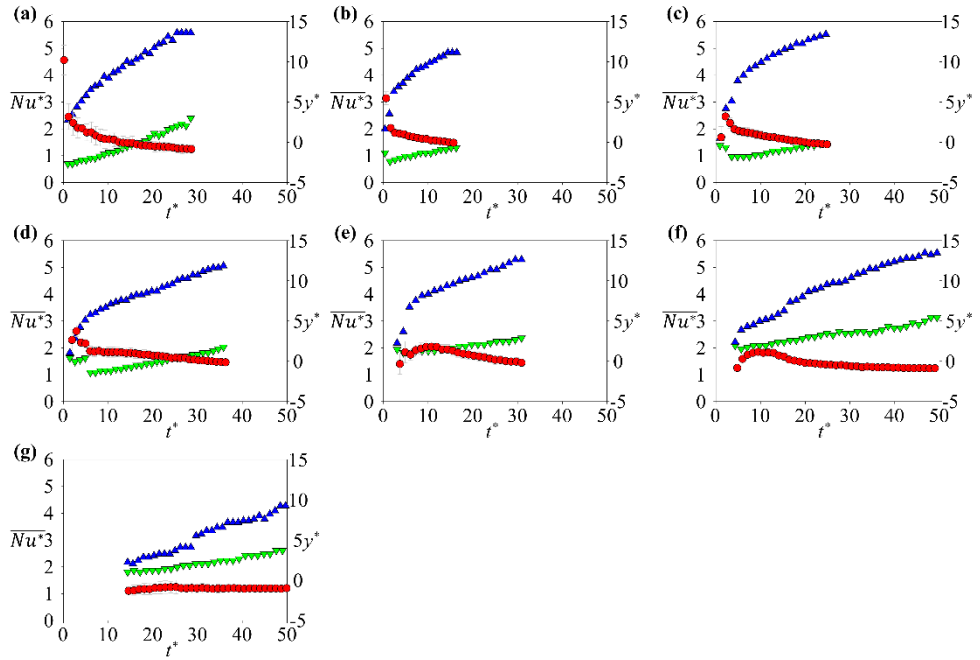


Figure 3.12. Upper (\blacktriangle) and lower (\blacktriangledown) boundary where the heat transfer is enhanced, and mean normalized Nusselt number in affected area (\bullet): $S^* = 0.5$ (a), $S^* = 1.5$ (b), $S^* = 2.4$ (c), $S^* = 3.2$ (d), $S^* = 4.5$ (e), $S^* = 5.1$ (f), and $S^* = 6.1$ (g).

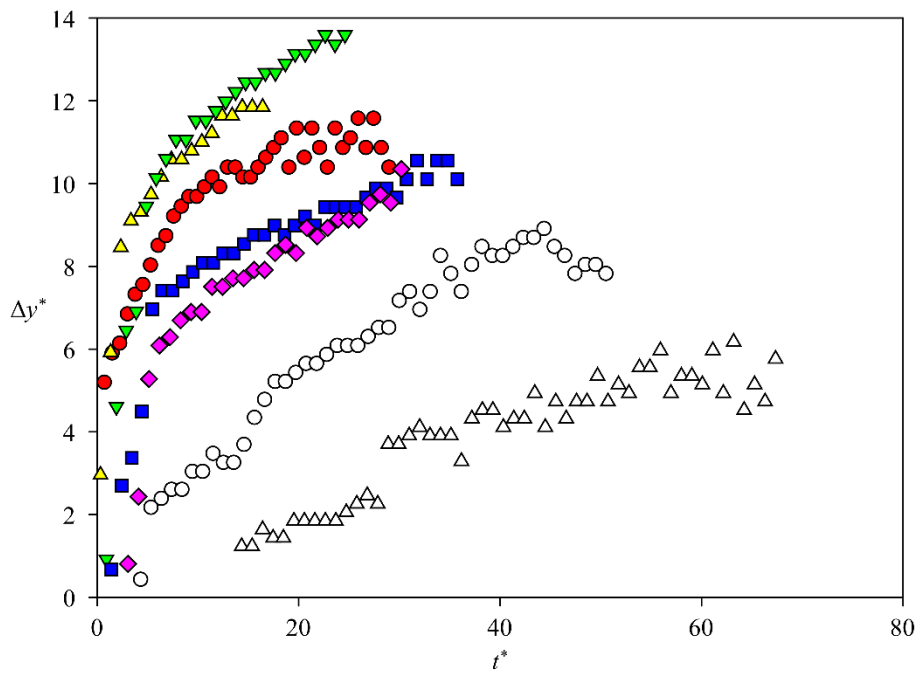


Figure 3.13. Normalized vertical width where the Nusselt number is increased: $S^* = 0.5$ (●), $S^* = 1.5$ (▲), $S^* = 2.4$ (▼), $S^* = 3.2$ (■), $S^* = 4.5$ (◆), $S^* = 5.1$ (○), and $S^* = 6.1$ (△).

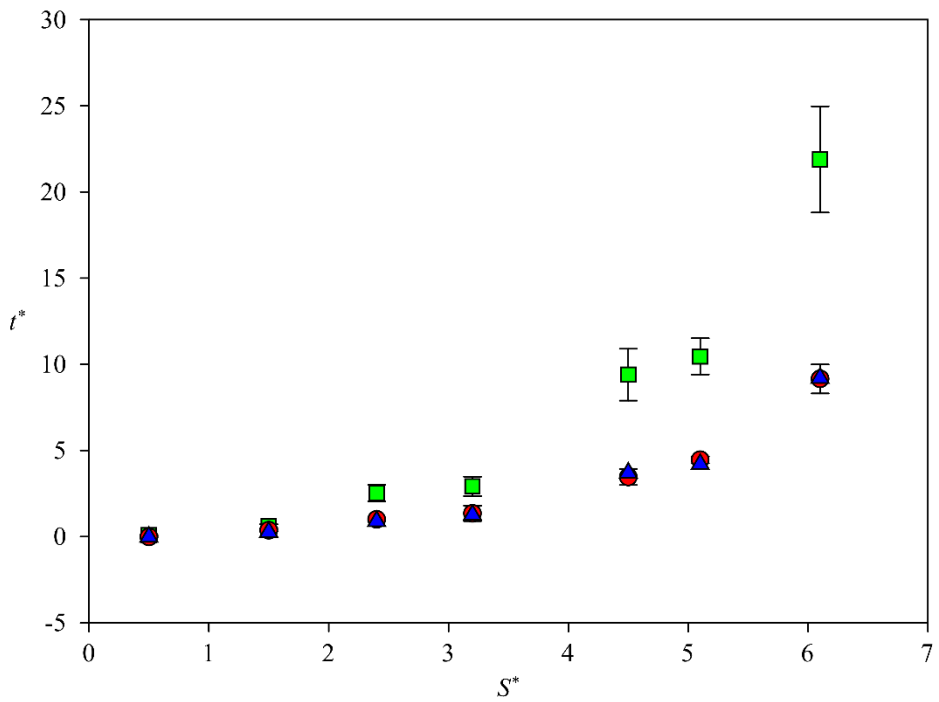


Figure 3.14. Normalized initial increment time of the Nusselt number (●), the normalized time that the vortex structure starts to contact with the wall (▲), and the normalized time when the instantaneous-local Nusselt number is the maximum (■) as a function of S^* .

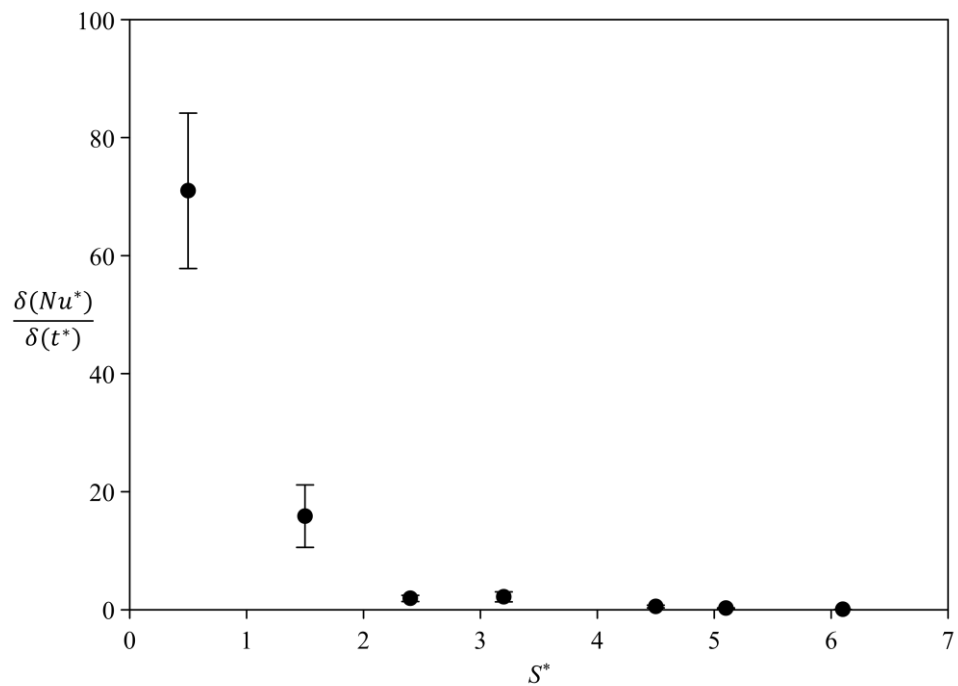


Figure 3.15. Normalized time gradient of the normalized Nusselt number, when the Nusselt number starts to increase, as a function of S^* .

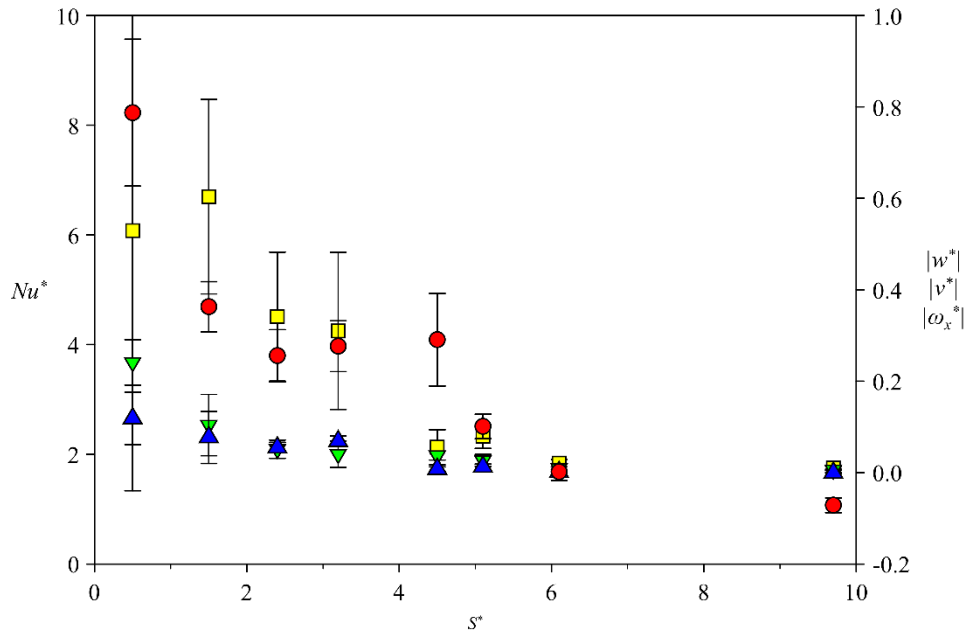


Figure 3.16. The normalized maximum Nusselt number (●), and normalized maximum strength of the wall normal velocity (▲), vertical velocity (▼) and vorticity (■) at zigzagging plane ($x = 0$), and fluid motions are measured at $0.2d_{eq}$ from the wall ($z^* = 0.2$), as a function of S^* .

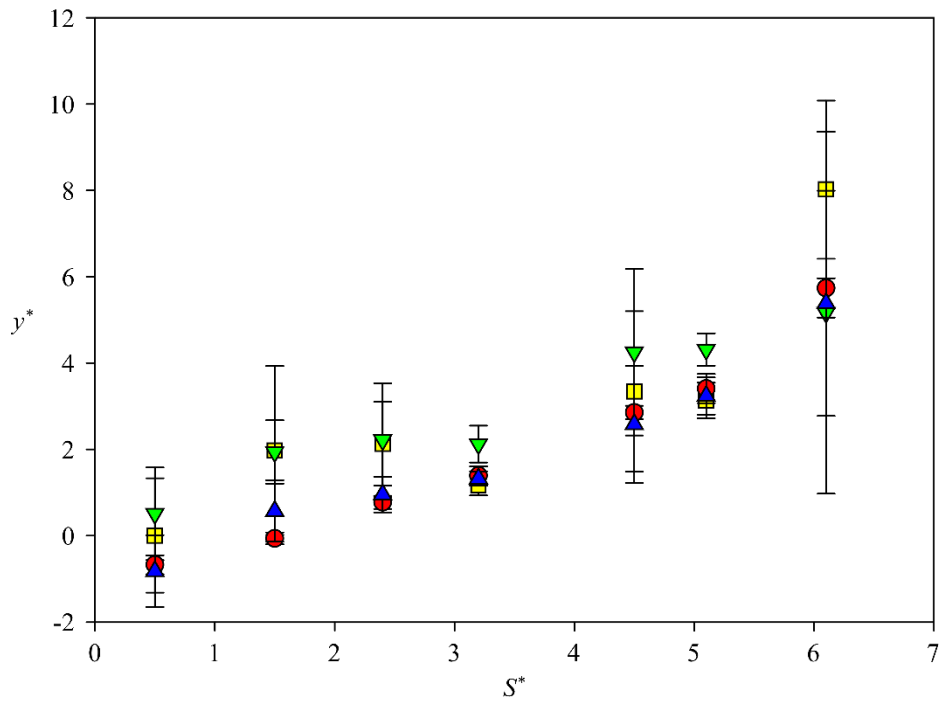


Figure 3.17. Normalized vertical position where the temporal-local Nusselt number or each of the local fluid component is maximized as a function of S^* : Nusselt number (\bullet), strength of the wall normal velocity (\blacktriangle), vertical velocity (\blacktriangledown) and vorticity (\blacksquare) at zigzagging plane ($x = 0$), and fluid motions are measured at $0.2d_{eq}$ from the wall ($z^* = 0.2$).

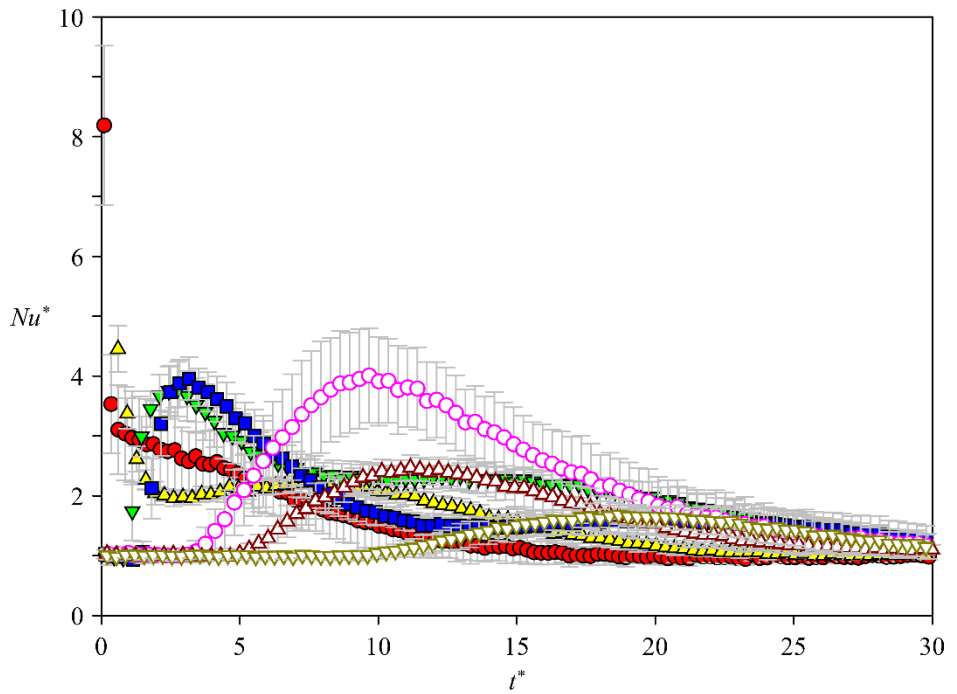


Figure 3.18. Normalized local-temporal Nusselt number (Nu^*) as a function of normalized time (t^*): $S^* = 0.5$ (●), $S^* = 1.5$ (▲), $S^* = 2.4$ (▼), $S^* = 3.2$ (■), $S^* = 4.5$ (○), $S^* = 5.1$ (△), and $S^* = 6.1$ (▽).

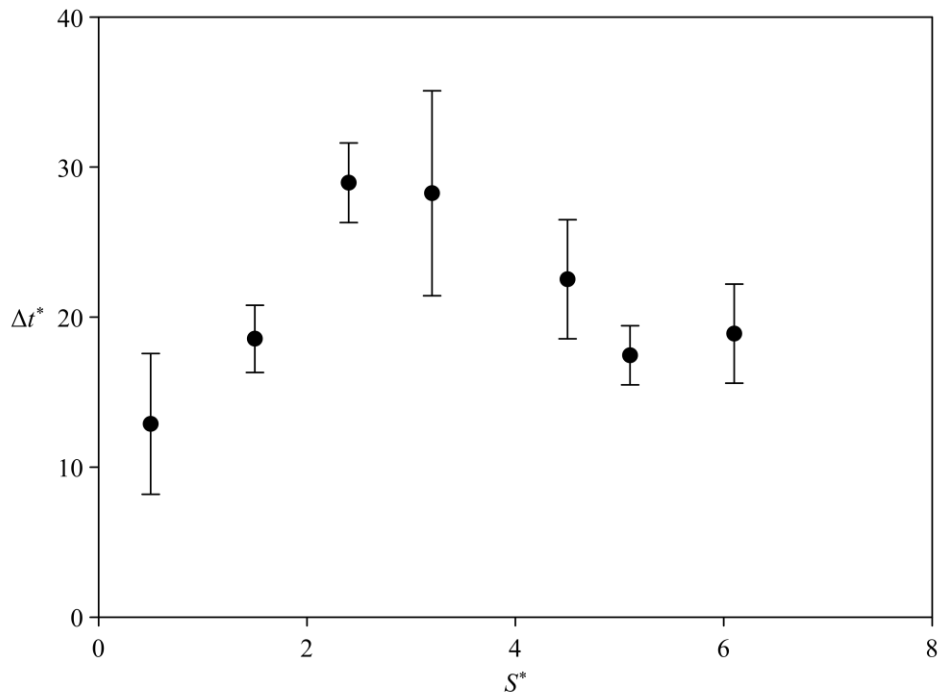


Figure 3.19. Normalized time duration of the Nusselt number increment at the vertical position where the temporal-local heat transfer coefficient is maximized at the centerline ($y = y_{max}^*$; $x = 0$).

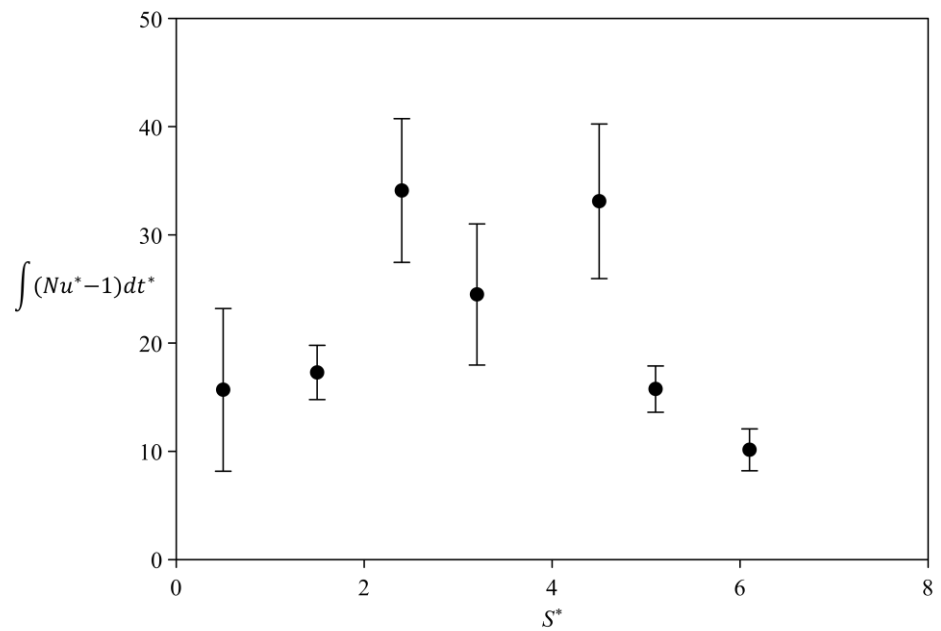


Figure 3.20. Integral value of the increased normalized Nusselt number ($Nu^* - 1$) over the whole normalized time.

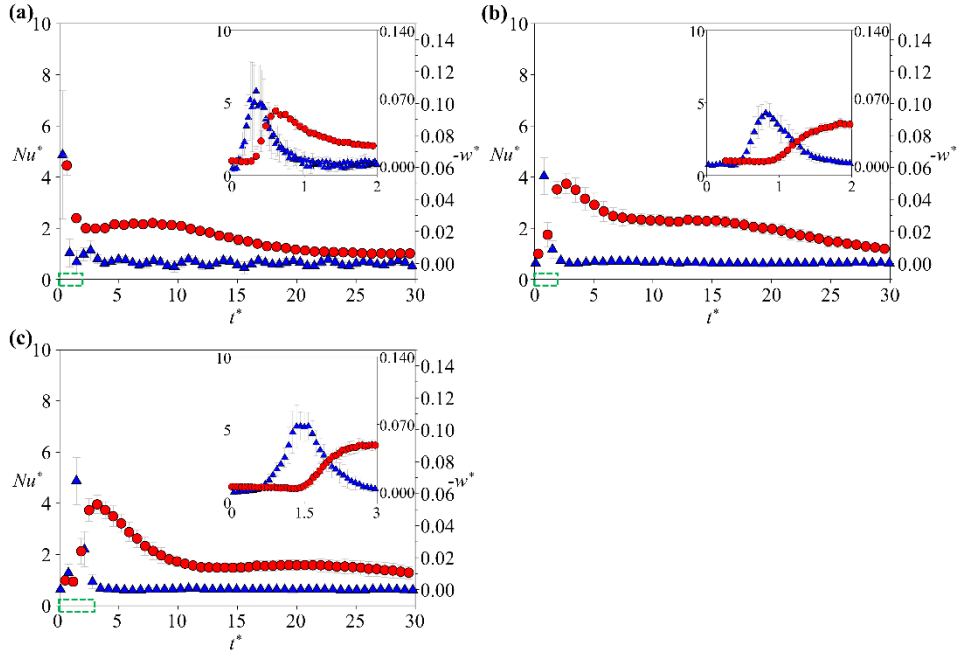


Figure 3.21. Nusselt number profile (●) where the heat transfer enhancement is maximized ($x = 0$, $y = y_{max}^*$, and $z = 0$), and wall-directional velocity profile (▲) near the wall ($x = 0$, $y = y_{max}^*$, and $z = 0.2d_{eq}$): $S^* = 1.5$ (a), $S^* = 2.4$ (b), and $S^* = 3.2$ (c), of which the cases where the Nusselt number increases again in the middle of decline. Domains corresponding to the green-dotted box on the time axis are magnified, which is plotted on the upper-right part.

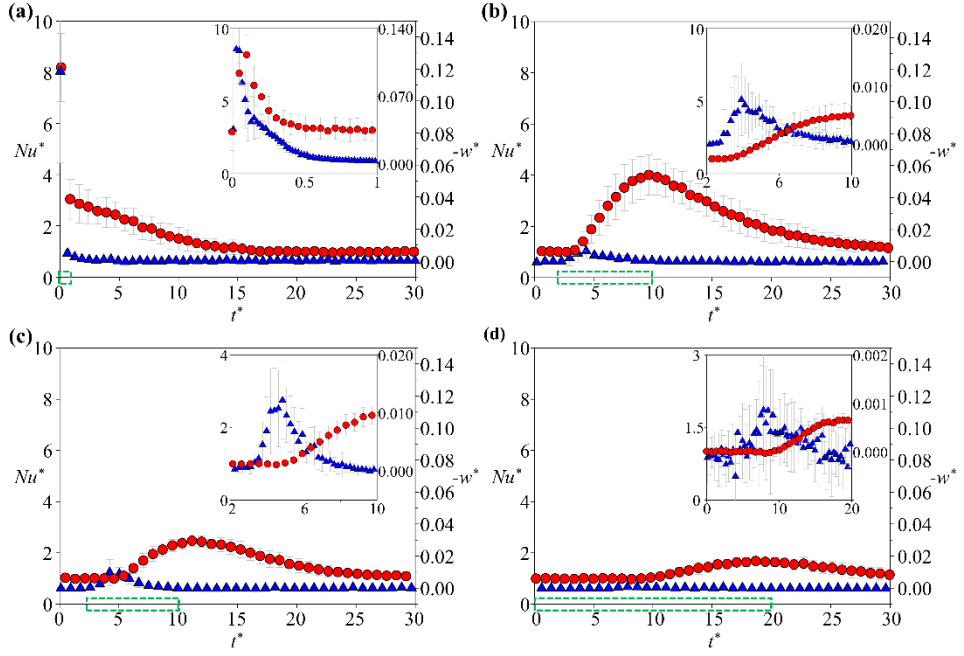


Figure 3.22. Nusselt number profile (●) where the heat transfer enhancement is maximized ($x = 0$, $y = y_{max}^*$, and $z = 0$), and wall–directional velocity profile (▲) near the wall ($x = 0$, $y = y_{max}^*$, and $z = 0.2d_{eq}$): $S^* = 0.5$ (a), $S^* = 4.5$ (b), $S^* = 5.1$ (c), and $S^* = 6.1$ (d), of which the cases where the Nusselt number decreases gradually after the enhancement. Domains corresponding to the green–dotted box on the time axis are magnified, which is plotted on the upper–right part.

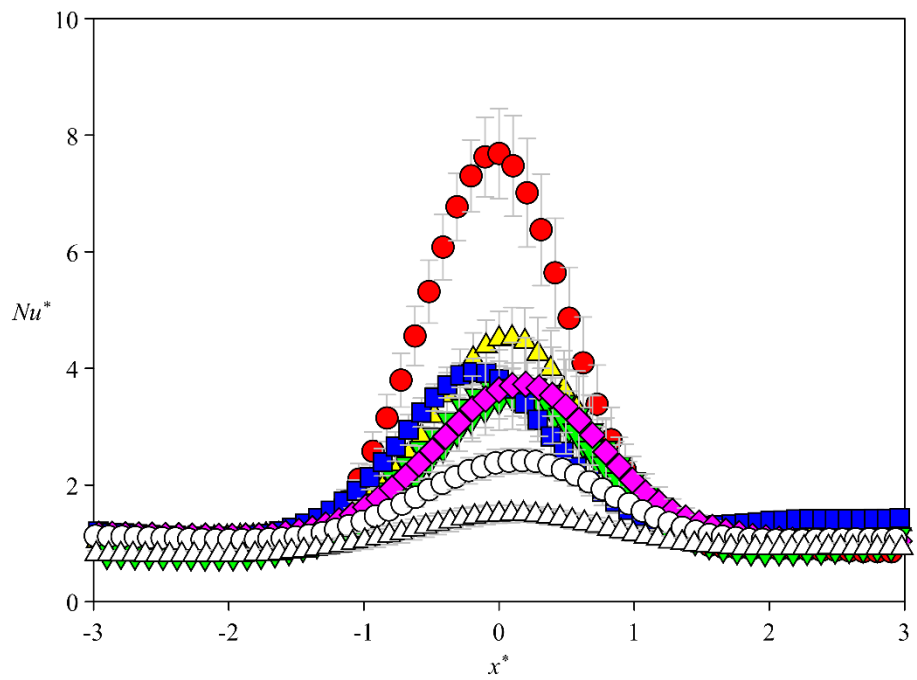


Figure 3.23. The maximum horizontal normalized Nusselt number at $y = y_{max}^*$: $S^* = 0.5$ (●), $S^* = 1.5$ (▲), $S^* = 2.4$ (▼), $S^* = 3.2$ (■), $S^* = 4.5$ (◆), $S^* = 5.1$ (○), and $S^* = 6.1$ (△).

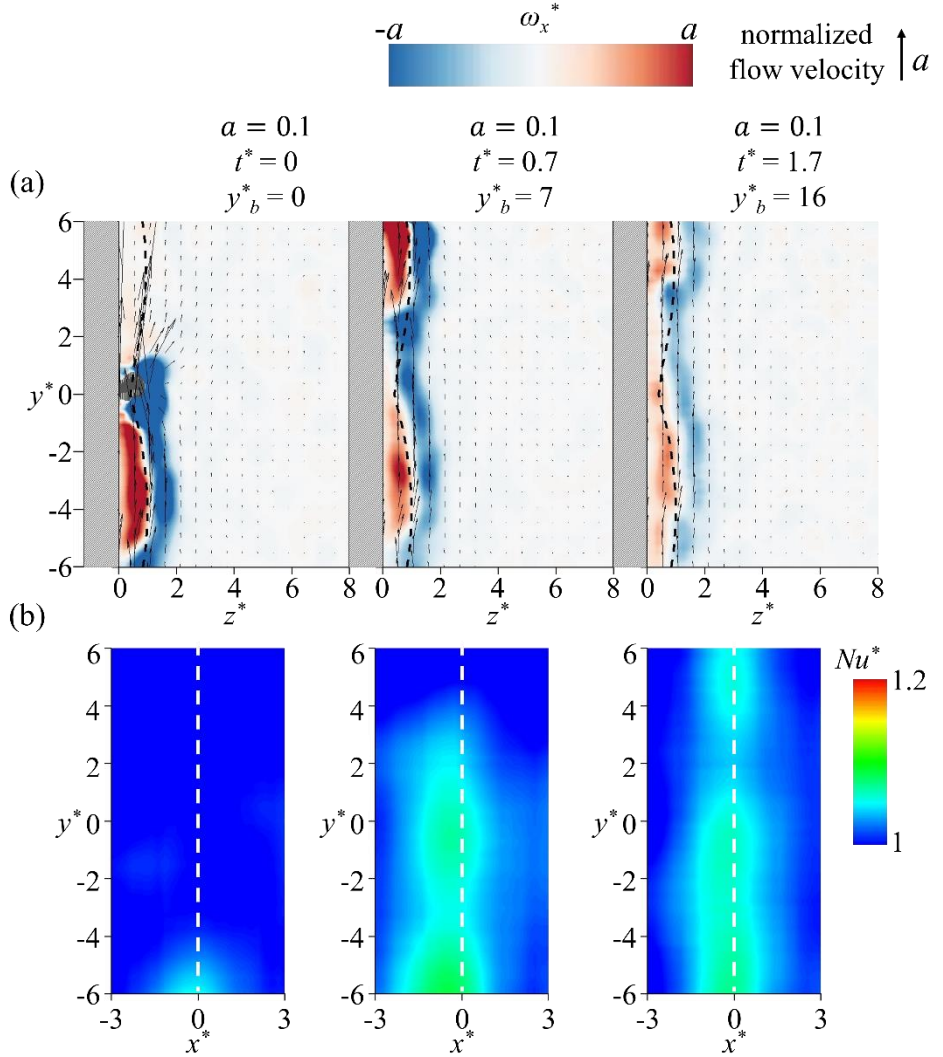


Figure 3.24. Temporal normalized spanwise vorticity (ω_x^*) field (a), and timely synchronized and normalized Nusselt number (Nu^*) field (b), which are timely synchronized, when bubble–wall distance (S^*) is 0.5 (bubble–wall collision; linearly–rising bubble). Here, a helps to describe normalized spanwise vorticity contour level and length of the unit vector, t^* denotes the normalized time, and y_b^* means the normalized vertical location of the bubble.

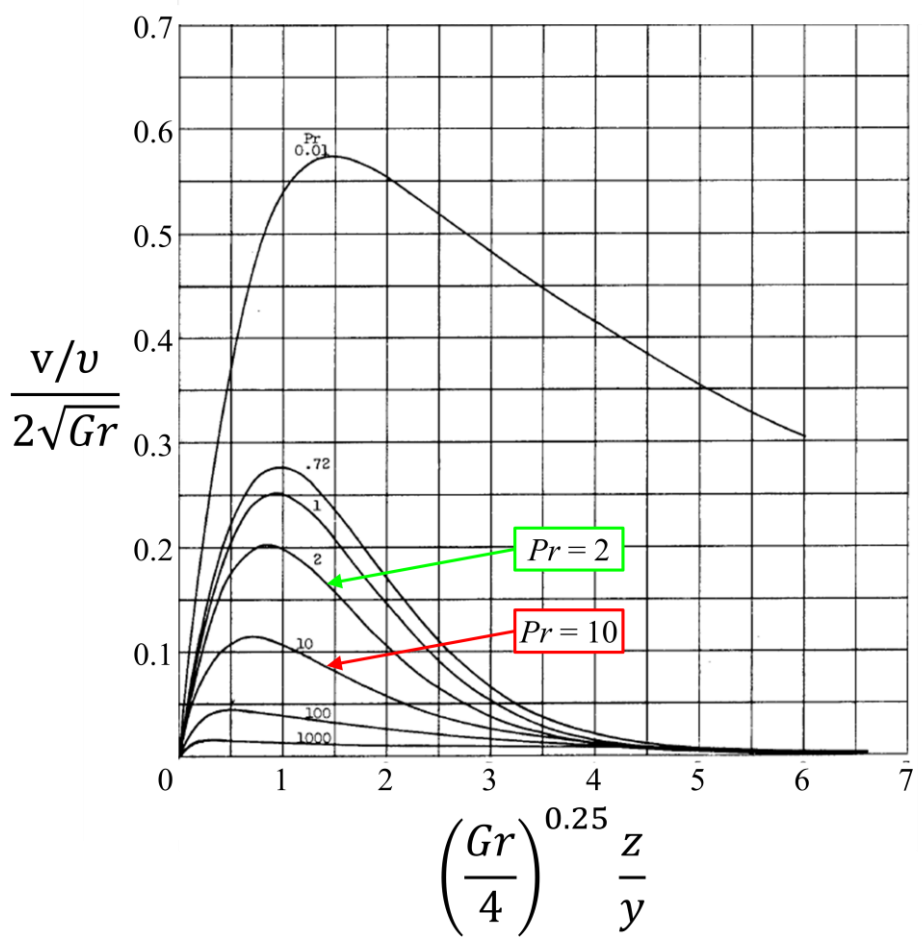


Figure 3.25. Dimensionless velocity distributions for various Prandtl numbers, which is reported by Ostrach, 1952.

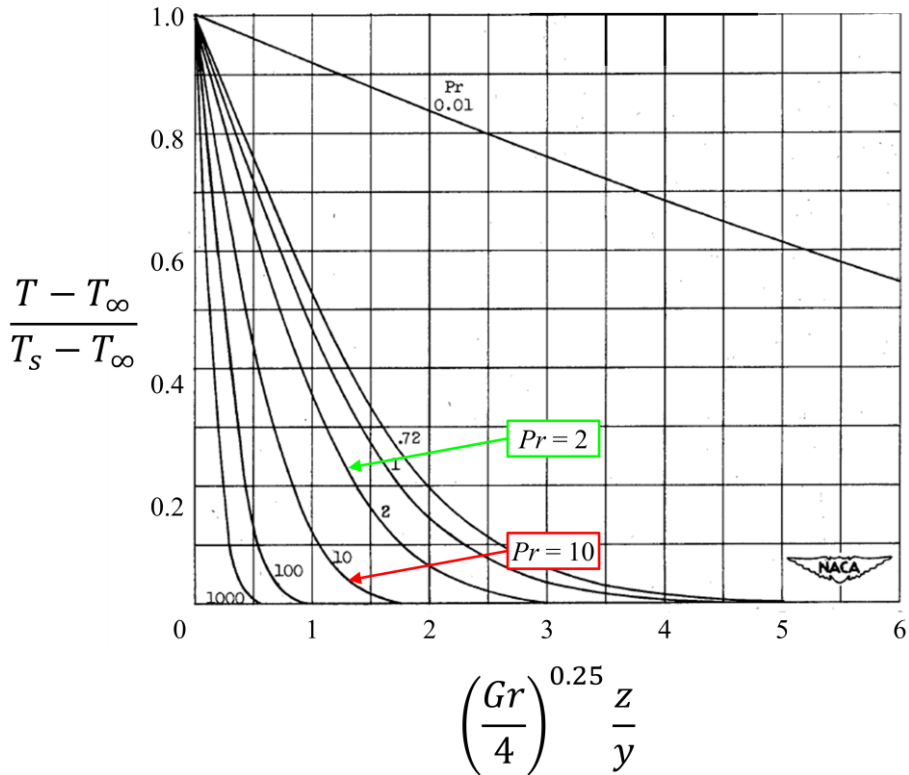


Figure 3.26. Dimensionless temperature distributions for various Prandtl numbers, which is reported by Ostrach, 1952.

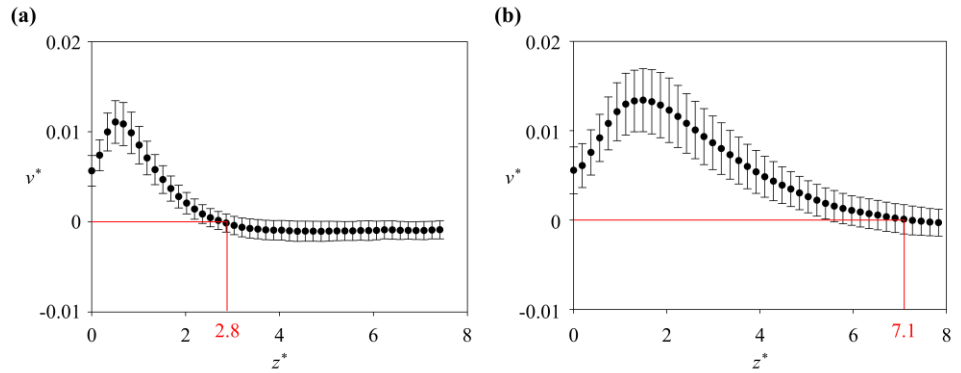


Figure 3.27. Normalized vertical velocity (v^*) profile along the normalized wall–normal direction (z^*): of the zigzag–rising bubble (a); of the linearly–rising bubble (b). Red solid line shows the location of z^* where the vertical velocity is zeros, which denotes the thickness of the momentum thermal boundary layer.

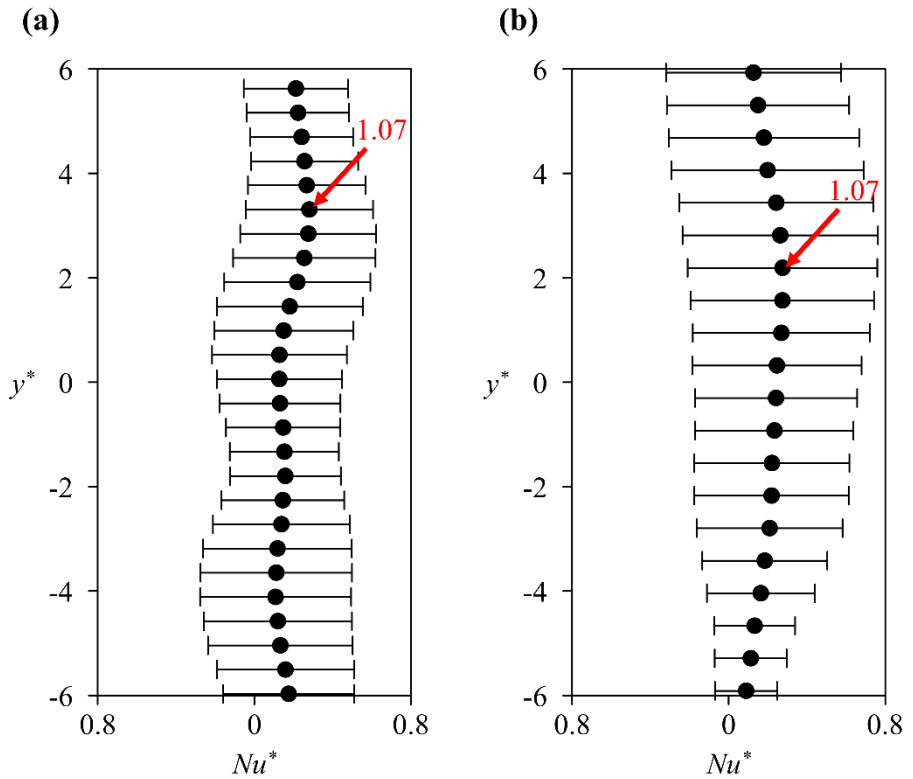


Figure 3.28. Vertical profile of the normalized Nusselt number when the spherical bubble periodically bounces (a) and when the spherical bubble initially bounces (b). The symbol denoted by the red arrow is the position where the temporal-local Nusselt number is maximized, and red number means the corresponding normalized Nusselt number.

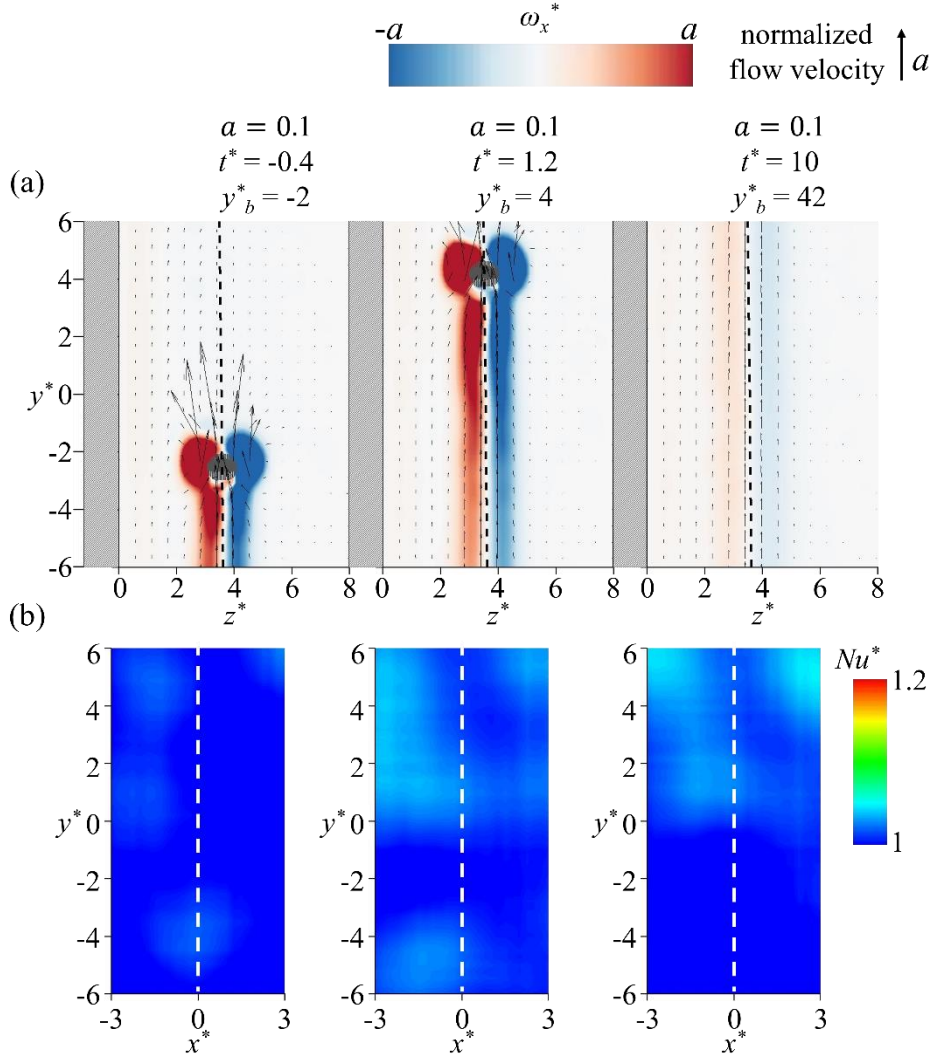


Figure 3.29. Temporal normalized spanwise vorticity (ω_x^*) field (a), and timely synchronized and normalized Nusselt number (Nu^*) field (b), which are timely synchronized, when bubble–wall distance (S^*) is 0.5 (no heat transfer; linearly–rising bubble). Here, a helps to describe normalized spanwise vorticity contour level and length of the unit vector, t^* denotes the normalized time, and y_b^* means the normalized vertical location of the bubble.

Chapter 4

Conclusion

In the present research, using a high-speed two-phased particle image velocimetry, we visualized temporal velocity field of the fluid, and by measuring the wall-temperature field, we calculated the amount of convective heat transfer, which are timely synchronized. With these techniques, we have experimentally investigated about the quantified growth rate of the heat transfer coefficient, and explained it by the visualized fluid velocity field. Also, by changing the bubble-wall distance, we have observed the distance effect on the variation of the Nusselt number. Moreover, by changing the bubble diameter, we compared the efficiency of each bubble for enhancing the heat transfer, which had a trajectory of straight and zigzag, which is determined by the Reynold number, Weber number and bubble-equivalent diameter.

When ellipsoidal-moderate sized bubble, which moves in zigzagging path, impinges on the wall, it directly entraines the bulk liquid, which increases the instantaneous local convective heat transfer up to eight times higher. Then, as it bounces off from the wall, vorticity accumulated behind the bubble is shed on the wall, and it mixes the fluid of the thermal boundary layer and enhances local heat transfer rate. For the case of increased S^* , the movement of a bubble is no longer interrupted by the wall, and several vortex structures are created at the rear part of a bubble. Vortex structures gradually convect to lateral direction and finally reach the wall, which renews the surface fluid. When the bubble-wall distance (S^*)

becomes further, some characteristics of heat transfer is changed: (i) the number of vortex structures which is able to arrive at the wall decreases, which means that the number of location where the local heat transfer is enhanced is declined; (ii) elapsed time from the moment when a bubble passes the summit point of the trajectory to the time when first Nusselt number increment occurs is become longer; (iii) normalized time gradient of the normalized Nusselt number gets smaller; (iv) the maximum instantaneous-local convective heat transfer rate decays; (v) the normalized vertical position where the maximum temporal-local normalized Nusselt number is induced (y_{max}^*) is increased. Although temporal-local heat transfer rate is decreased as the S^* becomes larger, timely integrated increased-normalized Nusselt number (Nu^*-1) at y_{max}^* is higher when there is moderate S^* : 2.4; 4.5. Moreover, by the Pearson correlation coefficient and p -value, we discovered that wall-normal velocity is most efficient flow component, which means the main mechanism of the bubble-induced forced convection is surface renewal. Additionally, horizontal affected area at y_{max}^* ranges over $3d_{eq}$, and had a Gaussian distribution.

Unlike the ellipsoidal zigzag-rising bubble, spherical straight-rising bubble is not efficient for enhancing the convective heat transfer, because: (i) vorticity and fluid velocity is weak; (ii) only single threaded wake is induced and dissipated without spread; (iii) size of the wake is evidently smaller than the thickness of the thermal boundary layer, which means that wake does not effectively entrain the bulk liquid to the wall.

Our study is meaningful in that simultaneous measurement of the flow velocity field and the convective heat transfer rate on the wall

by a single rising bubble is rarely done. Moreover, we will further develop this experiment by using laser induced fluorescence (LIF) technique, which visualizes the temperature field of the liquid phase. Also Bhuvankar et al., 2018 numerically studied about the heat transport when periodic bubbles rising near a vertical plate, and they discovered a recirculation zone between two bubbles. They reported the heat transfer mechanism in recirculation zone as the combination of suppressed heat transfer by upstream of the lower bubble and the increment of heat transfer by downstream of the upper bubble. Moreover, Gvozdic et al., 2018 investigated about the forced convective heat transfer by bubbly flow. They reported that heat transfer coefficient rises up to 20 times higher by bubbly flow when the gas volume fraction is 5% and the Rayleigh number ranges $4.0 \times 10^9 - 1.2 \times 10^{11}$. Therefore, further studies will be conducted in various bubble geometries like bubble chain or bubbly flow, where the different bubble induced flow and different heat transfer mechanisms would be observed.

Bibliography

- Aybers, N. M., & Tapucu, A. 1969, The motion of gas bubbles rising through stagnant liquid. *Wärme – und Stoffübertragung*, **2**, 171–177.
- Bhuvankar, P., & Dabiri, S. 2018, Impact of a single bubble rising near a wall on the wall-to-liquid heat flux. *Int. J. Heat Mass Transfer*, **116**, 445–457.
- Bongiovanni, C., Checaillier, J., & Fabre, J. Ph. 1997, Sizing of bubbles by incoherent imaging: defocus bias. *Exp. Fluids*, **23**, 209–216.
- Clifford, A.A. 1973, Multivariate error analysis: a handbook of error propagation and calculation in many-parameter systems. *John Wiley & Sons*.
- Curran-Everett, D., Benos, D. J. 2004, Guidelines for reporting statistics in journals published by the American Physiological Society. *J. Appl. Physiol.*, **97**, 457–459.
- Deen, N. G., & Kuipers, J. A. M. 2013, Direct numerical simulation of wall-to liquid heat transfer in dispersed gas–liquid two-phase flow using a volume of fluid approach. *Chem. Eng. Sci.*, **102**, 268–282.
- Delaure, Y. M. C., Chan, V. S. S., & Murray, D. B. 2003, A simultaneous PIV and heat transfer study of bubble interaction with free convection flow. *Exp. Therm. Fluid Sci.*, **27**, 911–926.
- Donnelly, B., Meehan, R. O., Nolan, K., & Murray, D. B. 2015, The

- dynamics of sliding bubbles and the effects on surface heat transfer. *Int. J. Heat Mass Transfer*, **91**, 532–542.
- Donoghue, D. B., Albadawi, A., Delaure, Y. M. C., Robinson, A. J., & Murray, D. B. 2014, Bubble impingement and the mechanisms of heat transfer. *Int. J. Heat Mass Transfer*, **71**, 439–450.
- Duineveld, P. C. 1995, The rise velocity and shape of bubbles in pure water at high Reynolds number. *J. Fluid Mech.*, **292**, 325–332.
- Ellingsen, K., & Risso, F. 2001, On the rise of an ellipsoidal bubble in water: oscillatory paths and liquid-induced velocity. *J. Fluid Mech.*, **440** 235–268.
- Fershtman, A., Shemer, L., & Barnea, D. 2016, Instantaneous heat transfer rate around consecutive Taylor bubbles. *Int. J. Heat Mass Transfer*, **95**, 865–873.
- Gibbons, J. D., & Chakraborti, S. 2003, Nonparametric statistical inference. *Marcel Dekker, Inc.*
- Gvozdic, B., Almeras, E., Mathai, V., Zhu, X., van Gils, D. P. M., Verzicco, R., Huisman, S. G., Sun, C., & Lohse, D. 2018, Experimental investigation of heat transport in homogeneous bubbly flow. *J. Fluid Mech.*, **845**, 226–244.
- Haberman, W. L., & Morton, R. K. 1953, An experimental investigation of the drag and shape of air bubbles rising in various liquids. *David W. Taylor Model Basin Report 802, U.S. Navy Dept.*
- Hartunian, R. A., & Martin, M. E. 1957, On the instability of small gas bubbles moving uniformly in various liquids. *J. Fluid Mech.*, **3**, 27–47.

- Hollingsworth, D. K., Witte, L. C., & Figueroa, M. 2009, Enhancement of heat transfer behind sliding bubbles. *J. Heat Transfer*, **131**, 121005–1–12005–9.
- Incropera, F. P., Witt, D. P. De., Bergman, T. L., & Lavine, A. S. 2007, Introduction to heat transfer. *John Wiley & Sons*.
- Jeong, H., & Park, H. 2015, Near-wall rising behavior of a deformable bubble at high Reynolds number. *J. Fluid Mech.*, **771**, 564–594.
- Jung, S., Kim, H. 2014, An experimental method to simultaneously measure the dynamics and heat transfer associated with a single bubble during nucleate boiling on a horizontal surface. *Int. J. Heat Mass Transfer*, **73**, 365–375.
- Kumar, S., Kusakabe, K., Raghunathan, K., & Fan, L. S. 1992, Mechanism of heat transfer in bubbly liquid and liquid–solid systems: Single bubble injection. *AICHE J.*, **38**, 733–741.
- Lawson, N. J., Rudman, M., Guerra, A., & Liow, J. L. 1999, Experimental and numerical comparisons of the break-up of a large bubble. *Exp. Fluids*, **26** 524–534.
- Lee, J., & Park, H. 2017, Wake structures behind an oscillating bubble rising close to a vertical wall. *Int. J. Multiphase Flow*, **91**, 225–242.
- Lindken, R., & Merzkirch, W. 2002, A novel PIV technique for measurements in multiphase flows and its application to two-phase bubble flows. *Exp. Fluids*, **33** 814–825.
- Meehan, R. O., Donnelly, B., Nolan, K., & Murray, D. B. 2017, Bubble–wake interactions of a sliding bubble pair and the mechanisms of

- heat transfer. *Int. J. Heat Mass Transfer*, **108**, 1347–1356.
- Ostrach, S. 1953, An analysis of laminar free-convection flow and heat transfer about a flat plate parallel to the direction of the generating body force, *NACA Report 1111*.
- Scammell, A., & Kim, J. 2015, Heat transfer and flow characteristics of rising Taylor bubbles. *Int. J. Heat Mass Transfer*, **89**, 379–389.
- de Vries, A. W. G. 2001, Path and wake of a rising bubble. *Doctorical thesis of Twente University*.
- de Vris, A. W. G., Biesheuvel, A., & van Wijngaarden, L. 2002, Notes on the path and wake of a gas bubble rising in pure water. *Int. J. Multiphase Flow*, **28**, 1823–1835.
- Willert, C. E., & Gharib, M. 1991, Digital particle image velocimetry. *Exp. Fluids*, **10**, 181–193.

국문 초록

본 연구에서는 수조 속 수직 열판 근처를 지나는 기포에 의해서 열판의 대류 열전달계수 변화를 정량적으로 측정하고, 그 메커니즘을 규명하였다. 수직 열판의 온도장은 적외선카메라를 통해서 측정되었고, 기포의 움직임과 후류는 초고속카메라를 통한 이상-입자유동영상계를 사용하여 측정되었으며, 두 카메라는 시간적으로 동기화되어 서로의 인과 관계를 설명하는데 사용되었다. 기포가 벽 근처를 지날 때 열판의 국소 열전달 계수가 증가하는 것을 확인하였으며, 벽과 기포사이의 거리를 변경하고, 기포의 크기를 변화시키면서, 이에 따른 열 전달 증가 효율 변화를 관찰하였다. 기포 지름이 2.8 mm 일 때는 기포가 지그재그의 움직임을 가졌고, 1.1 mm 일 때는 선형 움직임을 가졌다. 지그재그 기포가 벽에 충돌하는 경우에, 국소 열전달 계수는 순간적으로 8배까지 상승을 하였으며, 기포-벽 사이 거리가 멀어짐에 따라서, 순간적으로 증가되는 열전달 계수는 기하급수적으로 감소하는 경향을 보였다. 이 때, 기포에 의해 벽 근처에 유도되는 유동의 각 방향 최대 속도(벽과 수직한 방향, 벽과 수평한 방향)와 최대 와류도를 기포-벽 사이 거리에 따라 추출하였다. 각 유동 성분과 열전달계수 증가도의 유사도를 검증해본 결과, 열전달계수를 증가시키는데에는 벽과 수직한 방향의 속도성분이 가장 효율적임을 알았다. 이를 통해서 기포에 의한 수직 벽의 열 전달계수 증가의 주 원인은 외부의 찬물이 벽으로 끌려오는 현상임을 알게 되었다. 선형적으로 움직이는 기포는 열 전달 증가에 효율적이지 못함을 알게 되었는데, 기포가 벽과 충돌할 경우에는 10% 이하의 약한 열 전달 증가도를 보였고, 기포가 벽과 충돌없이 상승할 때에는 냉각효과가 없었다. 직선으로 상승하는 기포의 후류를 관찰한 결과, 지그재그로 움직이는 기포에 비해서 유동속도도 매우 느리고, 유동구조의 크기가 작은 것을 알 수 있었다. 일반적으로 알려진 충류 자유 대류 경계층 방정식과 측정된 유동장 정보로부터 온도 경계층 두께를 대략적으로 구해본 결과, 선형움직임

을 가지는 기포의 후류 유동구조는 온도경계층 두께보다 크게 작은 것을 알 수 있었다. 즉, 선형 움직임을 가지는 기포는 벽 근처의 따뜻한 물과 주변의 찬물 사이의 교환을 활발히 일으키지 못함을 발견하였다. 따라서, 기포를 통해 수직 열판의 대류 열전달을 활발하게 일으키기 위해서는, 벽에 강한 수직성분 유동을 유도하며, 그 유동구조의 크기가 온도 경계층 두께보다 큰 기포를 사용해야함을 발견하였다.

핵심어 : 상승기포, 그림자 이미지 기법, 입자 추적 속도 측정, 입자 이미지 속도 측정, 대류열전달, 누셀수

학번 : 2018-25231